# Mechanisms of the Overturning Circulation in the Northern Red Sea, more than Convective Mixing

Lina Eyouni[1,2], Zoi Kokkini [1,3], Nikolaos D. Zarokanellos [1,4], Burton H. Jones [1]

[1] King Abdullah University of Science and Technology (KAUST), Biological and Environmental Sciences and Engineering (BESE), Red Sea Research Center (RSRC), Thuwal, Saudi Arabia.

[2] Red Sea Global (RSG), Riyadh, Saudi Arabia.

[3] Consiglio Nazionale Delle Ricerche (CNR), Istituto di Scienze Marine (ISMAR), Lerici, Italy

[4] Balearic Islands Coastal Observing and Forecasting System (SOCIB), Palma de Mallorca, Spain

*Correspondence to*: Zoi Kokkini (zoi.kokkini@sp.ismar.cnr.it)

**Abstract.** The northern Red Sea (NRS) is where Red Sea Outflow Water (RSOW) and, occasionally, Red Sea Deep Water (RSDW), are formed. Glider observations are used to describe the formation mechanisms and pathways of the intermediate waters in the NRS in late winter from 31 January to 18 April 2019. Utilizing glider observations, atmospheric reanalysis products, and satellite datasets, we evaluated the mesoscale activity and the atmospheric conditions that contribute to outflow water formation. The cyclonic circulation in the region surfaces dense water, which exposes it to the atmosphere, ventilating the water column and contributing to phytoplankton growth (enhancement of chlorophyll concentration) due to the nutrients upwelled into the euphotic layer (Zeu). Subduction of this water in the 3-dimensional cyclonic circulation transported oxygenated, elevated chlorophyll water to depths between 150 m and 250 m along the 28.2 kg/m3 isopycnal. Unlike previous observations, in late February, a strong anticyclonic circulation blocked the inflow of warmer, fresher water into the region. It was accompanied by a negative heat flux and an uplifting of dense water to the surface. Net cooling through mid-March cooled the incoming surface waters from the south. At the end of the observational period, the intrusion of warmer, fresher waters from the south coincided with the re-establishment of cyclonic circulation and capped the dense surface water that had formed during March. These

28   observations demonstrate that multiple processes contribute to RSOW formation:  convective mixing,

29   cyclonic uplifting of dense water, subduction, and meso- (submeso-) scale processes.

## 1. Introduction

The Red Sea (RS) is a narrow, elongated, meridionally oriented basin lying between the Asian and African continents. Its subtropical location results in significant buoyancy losses due to high evaporation (nearly 2 m/yr), negligible precipitation, and effectively no riverine inputs, resulting in it being one of the world's saltiest and warmest seas (Edwards and Head, 1987; Smeed, 1997; 2004; Sofianos et al., 2002). The RS experiences seasonally reversing winds over the southern region, coupled with the Arabian Sea's monsoonal forcing. The reversing winds control the circulation and water mass exchange through the Strait of Bab al Mandab (Abualnaja et al., 2015; Patzert, 1974). These processes, along with the buoyancy forcing, drive the large-scale circulation (Bower and Farrar, 2015; Murray and Johns, 1997; Patzert, 1974; Sofianos and Johns, 2007). The inflow of water from the Gulf of Aden compensates for the evaporative water loss in the RS. The advected northward waters contribute to the overall latitudinal gradient in salinity and temperature from the south to the north. The northward advection of comparatively fresh and warm water from the south has an important role in the stratification (Asfahani et al., 2020; Churchill et al., 2014; Sofianos and Johns, 2007; Zarokanellos et al., 2017b), with the annual flux into the RS reaching up to 0.22 Sv (Sofianos and Johns, 2002). This water has been traced to the NRS at 28°N (Zarokanellos et al., 2017a). It is modified through heating, evaporation, and mixing as it progresses northward (Cember, 1988; Sofianos and Johns, 2003; Sofianos and Johns, 2007).

Significant mesoscale activity is found along the RS's main axis (Morcos, 1970; Morcos and Soliman, 1972; Quadfasel and Baudner, 1993; Sofianos and Johns, 2007; Zhan et al., 2014) that results from baroclinic instabilities (Zhan et al., 2014) and the presence of the Eastern Boundary Current (EBC; Zarokanellos et al., 2017a, 2017b; Biton et al., 2010; Biton et al., 2008; Bower and Farrar, 2015; Eshel et al., 1994; Eshel and Naik, 1997; Sofianos and Johns, 2007). Some of these mesoscale eddies are thought to be quasi-permanent features, in particular the cyclonic eddy (CE) in the Northern Red Sea (NRS) and the anticyclonic eddy (AE) in the Central Red Sea (CRS) (Chen et al., 2014; Yao et al., 2014b). The CE in the NRS plays a crucial role in forming the RSOW (Asfahani et al., 2020; Sofianos and Johns, 2007). Zarokanellos et al. (2017a) have shown that an AE in the CRS can redirect or deflect the advected northward flow of Gulf of Aden water. These mesoscale eddies substantially affect heat and salt advection and distribution of biogeochemical properties (Chen et al., 2014; Raitsos et al., 2013; Triantafyllou et al.,

3

58  2014), which are often useful tracers of physical processes. Eddies also transfer energy and momentum

59  to the mean flow, driving the circulation (Lozier, 1997). In addition, mesoscale features fundamentally

60  modulate local nutrient fluxes and phytoplankton dynamics (Longhurst, 2007). Eddy activity in the RS

61  has shown that it significantly influences the optical and biological properties (Kürten et al., 2016;

62  Mahadevan, 2015; McGillicuddy et al., 1998; Pearman et al., 2017; Siegel et al., 2008). In particular,

63  mesoscale eddies in the RS facilitate the vertical transport of nutrients into the upper water column,

64  thereby impacting biogeochemical variability (Zarokanellos et al., 2017; Kürten et al., 2019).

65  Mesoscale processes can induce subduction events over larger areas with significant impact in the

66  marine ecosystem (Mahadavan et al. 2016). Subduction is the process where physical and biogeochemical

67  tracers transport from the surface to the interior. This, in turn, influences the chlorophyll flux in the Zeu

68  playing a significant role in the RS biological variability. Furthermore, while the upper ocean is primarily

69  ventilated through subduction events, the ventilation in the deep ocean occurs primarily through open-

70  ocean convection (Asfahani et al., 2020; Williams and Meijers 2019). Seasonal mixing, eddy interactions,

71  and cross-shelf exchange drive biogeochemical fluxes in the upper layer. In the RS, seasonal

72  phytoplankton variability has been studied primarily through remote sensing (Acker et al., 2008; Gittings

73  et al., 2018; Racault et al., 2015; Raitsos et al., 2013), with only a few studies incorporating in situ

74  observations (Kheireddine, 2020; Zarokanellos et al., 2017a, 2017b; Zarokanellos & Jones, 2021). These

75  studies highlight ecological connections between coastal and open-sea regions, vital for coral

76  communities (Acker et al., 2008; Raitsos et al., 2017). However, remote sensing is limited to surface

77  observations, as ocean color data do not capture subsurface phytoplankton distributions.Integrating bio-

78  optical data from both remote sensing and in situ measurements has provided valuable insights into the

79  RS's biogeochemical dynamics (Brewin et al., 2015; Gittings et al., 2018; Kheireddine et al., 2020;

80  Racault et al., 2015; Raitsos et al., 2013; Tiwari et al., 2018; Zarokanellos et al., 2017a, 2017b;

81  Zarokanellos & Jones, 2021).

82  Water mass transformation typically occurs in the surface ocean in specific regions where air-sea

83  interaction acts powerfully on the upper layer (Emery, 2001; Iselin, 1939). Significant surface cooling

84  results in buoyancy loss that can contribute to deep mixing and convection. The NRS has been considered

85  the main area of RSOW formation and, occasionally, Red Sea Deep Water (RSDW) formation

(Papadopoulos et al., 2015; Sofianos and Johns, 2003; Sofianos and Johns, 2007; Yao et al., 2014 b), due to the high evaporation rates and significant surface water cooling that occur during winter (Papadopoulos et al., 2013). These preconditions, in addition to the presence of the CE, where shallowing of the isopycnals occurs at the eddy center, contribute to the formation of the aforementioned RSOW and RSDW (Abualnaja et al., 2015; Asfahani et al., 2020; Sofianos and Johns, 2003; Yao et al., 2014 b; Zhai et al., 2015). The newly formed RSOW gradually sinks until it reaches an equilibrium density of near 27.5 to 27.7 kg/m$^3$ throughout the basin (Zhai et al., 2015) and flows southward, where it exits the RS through the strait of Bab-El-Mandeb (Cember, 1988; Sofianos and Johns, 2003; Yao et al., 2014 b). Once it enters the Gulf of Aden, it is mixed due to the intense mesoscale eddy activity at depths between 400 and 1000 m (Bower and Furey, 2010). Despite significant dilution of the thermohaline properties, RSOW has been observed as far southward as the Agulhas Current below 32˚S (Beal et al., 2000) and as far east as the Bay of Bengal (Jain et al., 2017).

Numerical simulations and a few in-situ observations suggest three potential mechanisms for RSOW formation. The first mechanism, open-ocean convection, is associated with the presence of a cyclonic gyre in the NRS (Sofianos and Johns, 2007; Papadopoulos et al., 2015). Strong atmospheric forcing in the region and the presence of cyclonic gyre creates favourable conditions for convection events. The second mechanism is mixed layer deepening during winter, resulting from a large negative heat flux (Zhai et al., 2015). The third mechanism is the combined effect of the cyclonic gyre and the weakening of the stratification that results from strong atmospheric forcing (Chen et al., 2014; Clifford et al., 1997; Manasrah et al., 2004; Morcos and Soliman, 1972; Yao et al., 2014 b). Concurrent with the formation of the RSOW, the RSDW forms in the NRS when strong cooling and evaporation occur in the gulfs of Suez and Aqaba (Cember, 1988; Papadopoulos et al., 2015; Sofianos and Johns, 2003; Yao et al., 2014 b). The RSDW is evident below 300 m, while the RSOW is typically found between 200 and 300 m and can be identified by the relatively high oxygen concentration, which can be distinguished from the RSDW. The regionally formed RSOW has a significant role in the overturning circulation, as indicated by in-situ observations and numerical simulations (Papadopoulos et al., 2015; Sofianos and Johns, 2003; Zhai et al., 2015). In addition, RSOW contributes to the ventilation of the RS (Papadopoulos et al., 2015; Sofianos

113 and Johns, 2007; Woelk and Quadfasel, 1996; Yao et al., 2014 b; Zhai et al., 2015) and the salt budget of
114 the Indian Ocean due to the high salinity concentrations present in intermediate depths (Beal et al., 2000).
115     The primary objective of this study is to understand the mechanisms that contribute to the mass
116 formation of RSOW in the NRS and the biogeochemical responses associated with these physical
117 processes. The second objective is to evaluate how atmospheric forcing affects mesoscale dynamics in
118 the study area. This paper is organized as follows: In Section 2, the in-situ, reanalysis, and remote sensing
119 observations are presented. Section 3 describes the coupling of the atmospheric forcing and the in-situ
120 observations. A comprehensive description of the flow variability and the mechanism of RSOW
121 formation is described, including the coupling between physical and biogeochemical processes in the
122 study area. Finally, Section 4 presents a discussion and comparison with previous regional studies, along
123 with the conclusions.
124

**2. Data and methods**

**2.1 Glider observations**

A sustained glider line that was traversed in a 3-4 day period in the NRS was used to capture the wintertime evolution of physical and biogeochemical characteristics in the NRS (Eyouni et al., 2024). The Seagliders (hereinafter "gliders") were equipped with a CTD, a dissolved oxygen sensor, and a triplet fluorometer (**Table 1**). The glider was deployed along a transect oriented approximately perpendicular to the coastline offshore from Duba, referred to as the "Duba line" (**Fig. 1a**). The line extended from approximately 5 km off the coast to nearly 75 km offshore. The glider completed each transect in about 3.5 days and was programmed to dive from the surface to ~750 m. The average horizontal speed was ~25 cm/s, and each dive cycle took ~3 hours to complete, depending on the target depth, topography, and sea conditions. The deployment spanned the period from 31 January to 21 April, 2019 (**Table 1**, **Fig. 1b**).

| Deployment Location | Observation Period | Duration (days) | Sensors | Parameter |
|---|---|---|---|---|
| | | | Seabird, unpumped CT | CTD (Conductivity, Temperature, Pressure) |
| NRS | 30.01.2019/22.04.2019 | 83 | WETlabs EcoPuck Fluorometer (FL3-IRB sensor) | Chlorophyll Fluorescence ( CHL),Colored Dissolved Organic Matter (CDOM),Phycocyanin |
| | | | WETlab Backscatter (BB3 IRB sensor) | Backscatter at 532, 650, and 880 nm |

| | | | Aanderaa Optode (4330) | Dissolved Oxygen (DO) |
|---|---|---|---|---|
| | | | | |

137

138    **Table 1:** Summary of the measured variables and their corresponding sensors deployed on the glider.
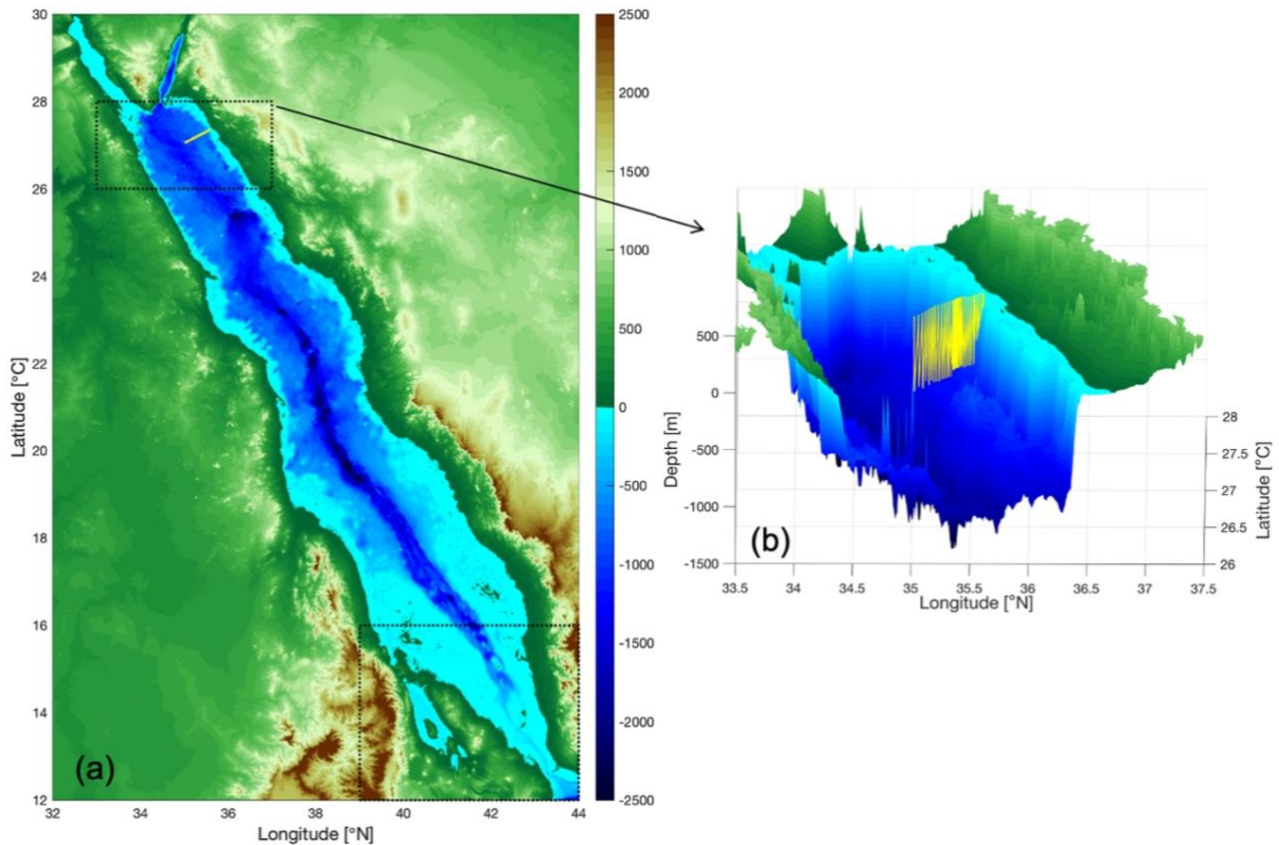
**Fig. 1:** Topographic map of the RS. The two black dash boxes in the northern and southern RS show the study area in the north and the region in the south where exchange with the Gulf of Aden occurs. The yellow line inside the northern box indicates the glider line location, and b) the yellow sawtooth line represents the undulating trajectory of the glider superimposed on the bathymetry, which has been reproduced from the GEBCO_2021 Grid, GEBCO Compilation Group (2021; https://doi.org/10.5285/c6612cbe-50b3-0cff-e053-6c86abc09f8f).

Each vertical profile has been examined for spikes and outliers before further analysis. No evidence of thermal lag has been observed in the CT observations. The WETlabs EcoPuck Triplet Fluorometer (FL3) and backscatter (BB3) sensor were factory calibrated, and dark counts were measured prior to

9

deployment to account for any drift. However, the BB3 sensor starts to drift on 26 March 2019. The pre-deployment dark counts for the FL3 were consistent with factory dark counts. Roesler et al. (2017) performed a global comparison of fluorometer and extracted CHL measurements and recommended that factory-calibrated chlorophyll should be divided by two. Thus, here CHL is divided by 2 to correspond to in situ CHL concentrations as described in Roesler et al. (2017). As the RS is a region with high irradiance, the CHL can often experience quenching. In this study, we examined the vertical profiles of CHL fluorescence for quenching, and no significant quenching was detected. The oxygen measurements were adjusted by a correction factor based on the median oxygen saturation in the upper 10 m. The correction factor was the ratio of the median oxygen saturation concentration for the upper 10 m to the median measured concentration within the upper 10 m of the water column. The entire water column data was then corrected by multiplying the reported oxygen concentrations by the correction factor. The correction provided consistency between the current glider data set and the vertical distribution for this region in the World Ocean Atlas (Zarokanellos and Jones, 2021; Garcia et al., 2019a). To facilitate data processing, plotting, and analysis, the corrected data were projected onto a grid with a vertical resolution of 2 m and a horizontal resolution of 2.5 km, the nominal distance between glider surfacing during the mission. This study focuses on the upper 500 m of the water column. Mixed Layer Depth (MLD) was calculated for each vertical profile based on a density difference of $\leq 0.03$ kg/m3 relative to the density at 10 m depth (de Boyer Montégut et al., 2004). The Brunt-Vaisala frequency (BVF) was computed to measure stratification. Geostrophic velocity and potential density were also calculated using the TEOS-10 toolbox (TEOS, SCOR, and IAPSO, 2010). The level of no motion in the geostrophic velocity has been examined, and no significant motion below 500 m has been observed.

## 2.2 Remotely sensed data

### 2.2.1 Sea Level Anomaly (SLA)

Previous satellite observations and numerical simulation studies suggest a cyclonic gyre located in the NRS concurrent with convective mixing where the RSOW water mass is formed (Sofianos and Johns, 2002; Zhai et al., 2015). Therefore, in this study, SLA data were used to characterize the spatial and temporal evolution of the large-scale circulation patterns of sea level and geostrophic velocity during the

179 wintertime. The SLA data is based on the multi-mission altimeter Archiving Validation and Interpretation

180 of Satellite Oceanographic Data (AVISO) provided by the Copernicus Marine Environment Monitoring

181 Service (CMEMS). The data has been gridded at a regular 0.258˚ X 0.258˚. The obtained daily measured

182 data were taken within the domain from 20˚ to 28˚ N and 32˚ to 42˚ E, inclusive of the glider deployments.

183 Within the NRS subdomain (26 - 28 ˚N, 33 - 37 ˚E), the data were temporally averaged to fit approximate

184 the periods of the glider transects. Previous work has validated the use of the AVISO product from

185 comparisons with both in situ and numerical model results (Hernandez and Schaeffer, 2001; Zhan et al.,

186 2014; Zarokanellos et al., 2017).

187

188 **2.2.2 Sea Surface Temperature (SST)**

189 Sea surface temperature (SST) data were obtained from the Moderate Resolution Imaging

190 Spectroradiometer (MODIS) imagery that provides a daily image with a spatial resolution of 4 km. The

191 data were obtained within the domain from 24˚ to 28˚ N to identify and determine the spatial and temporal

192 evolution of the large-scale patterns of the SST (Werdell et al., 2013).

193

194 **2.3 Atmospheric reanalysis products**

195

196 Atmospheric parameters for this study were derived from the Modern-Era Retrospective Analysis for

197 Research and Applications Version 2 (MERRA-2) reanalysis dataset (Rienecker et al., 2011; Gelaro et

198 al., 2017). MERRA-2 offers a high-resolution representation of atmospheric conditions, providing daily

199 mean values on a $0.5° \times 0.652°$ grid with a temporal resolution of one hour. This dataset was chosen due

200 to its demonstrated accuracy in representing heat fluxes within the region of interest, as validated by

201 recent studies such as Al Senafi et al. (2019). For this analysis, data were extracted and spatially averaged

202 over a defined box encompassing the NRS (NRS26 - 28 ˚N, 33 - 37 ˚E; **Fig. 1a**), excluding land coverage.

203 Daily means were calculated from the hourly data for the selected parameters of wind speed and direction,

204 surface net heat flux ($Q_{net}$), and evaporative heat flux, which is considered to be the primary driver of

205 heat loss in the RS (Sofianos ad Johns, 2003).

206　The $Q_{net}$, produced using the Coupled Ocean-Atmosphere Response Experiment (COARE 3.0)

207　formulation (Fairall et al., 1996), consists of the sum of shortwave (Q_sw, absorbed), longwave (Q_lw,

208　emitted), latent (Q_L, evaporative), and sensible (Q_s, conductive) heat fluxes, as all terms are positive when

209　they are heating the water column. The quantity $Q_{net}$ is calculated using the following formula:

210

211　　$Q_{net} = Q_{sw} + Q_{lw} + Q_S + Q_L$　　　　　　　　　　　　　　　　(1)

212

213　**2.4 Empirical Orthogonal Function (EOF) analysis**

214　To compare the SLA from 2019 with observations from the preceding years, EOF analysis is carried

215　out on SLA data to evaluate the spatial and temporal patterns of the variability of the SLA data in the

216　winter-spring period. Each eigenvector describes the spatial pattern (modes) of that variability for five

217　months of January to May for the years 2016, 2017, 2018, and 2019. Only the first mode of the EOF is

218　used to compare the seasonal evolution of the spatial pattern each year. In addition, the explained variance

219　with the eigenvalue provides the relative contribution that a specific mode contributes to the variability

220　(Zhang and Moore, 2015).

221

222　**2.5 One-dimensional mixed layer model**

223　Price-Weller-Pinkel (PWP) mixed layer model (Price et al., 1986) has been applied to evaluate the

224　local atmospheric effects on the ocean mixed layer. The. The model input includes the following terms:

225　radiative heat flux (shortwave, longwave), latent and sensible heat, freshwater flux (evaporation [E] and

226　precipitation [P]; [$E - P$]), and wind stress components [$\tau_x and \tau_y$]). As the RS is sandwiched between

227　two extreme desert regions, precipitation is considered to be negligible (P=0). The 1-D PWP has been

228　applied to estimate the local, atmospherically-driven evolution of the mixed layer depth during the

229　observation period. The model was executed for three sequential subsets delineated from the glider

230　observations: the cooling phase, the cool, salty, dense phase, and the warming-freshening phase. The

231　model was initialized with the average temperature and salinity profile for one complete glider transect

232　at the beginning of each simulation period (30 days) and then stepped forward in 24-hour (1-day)

233    increments subject to the heat, freshwater, and momentum fluxes. The daily time step was selected as

234    insignificant diurnal variability was observed in mixed layer temperature and salinity from the glider.

235    The PWP model produces a mixed layer through a vertical exchange process between the air and sea

236    interaction and vertical mixing. It assimilates time series of surface heat flux, wind, and precipitation and

237    applies these forcing parameters to the initial vertical profile of temperature and salinity. The model

238    interpolates the momentum components driven by winds, cooling, and evaporation to induce convective

239    instability, entrainment from the pycnocline, and a mixing term generated from vertical current shear. In

240    our case, since P=0, only surface heating affects re-stratification.

241    The convective adjustment in the PWP model starts with grid cells with unstable stratification being

242    homogeneously blended with neighbouring cells. The convective correction follows the bulk mixed layer

243    parameterization, where the mixed layer deepens when the bulk Richardson number, $R_{ib}$, falls below a

244    threshold value of 0.65 (Price et al., 1986).

245    The bulk Richardson number is expressed as: $R_{ib} = \frac{\Delta \rho g}{\rho_0 (\Delta U)^2}$      (2)

246    where $\Delta\rho$ (density) and $\Delta U$ ($velocity$) are the differences between their values within the mixed layer,

247    and their values below the mixed layer, respectively (Price et al., 1986). The variable $\rho_0$ is the reference

248    density and $g$ is the gravitational acceleration. Then, the model adds local shear instability below the

249    mixed layer, where mixing due to strong shear is parameterized based on a threshold gradient Richardson

250    number, $R_{ig}$, defined as: $R_{ig} = \frac{N^2}{S^2} = 0.25$      (2a)

251    where, $S^2$ is the square of the shear below the mixed layer and $N^2 = \frac{g}{\rho}\frac{\Delta\rho}{\Delta z}$      (2b)

252    The vertical resolution of the model depth bin was set to 2 meters to be aligned with the gridded glider

253    data. The momentum (horizontal diffusivity) and vertical diffusivity were set to $10^{-5}$ m$^2$/s and 0 m$^2$/s,

254    respectively (Sanikommu et al, 2020; Zhai et al., 2015). The maximum depth of the PWP experiment for

255    the run and the initial depth range for the profiles of salinity and temperature were 400 m, the depth at

256    which the divergence of hydrographic variables between summer and winter was minimal. Estimation of

257    the MLD at each time step throughout the PWP model run used the same criteria used for the glider data

258    by determining the depth range over which the density increase relative to 10 m was no more than 0.03

259    kg/m$^3$ (de Boyer et al., 2004).

260

## 3. Results

### 3.1 Atmospheric forcing

Regional atmospheric forcing is a major factor affecting the seasonal variability of the RS circulation. The wind direction in the northern part of the RS is predominantly from the north-northwest (NNW; **Fig. 2a**). The net heat flux was initially negative, with heat flux losses of up to 300 w/m$^2$ in January, up to 250 w/m2 in February, and transitioning in late March from net negative to net positive, thus beginning the onset of the seasonal heating period (**Fig. 2b**).



268

14
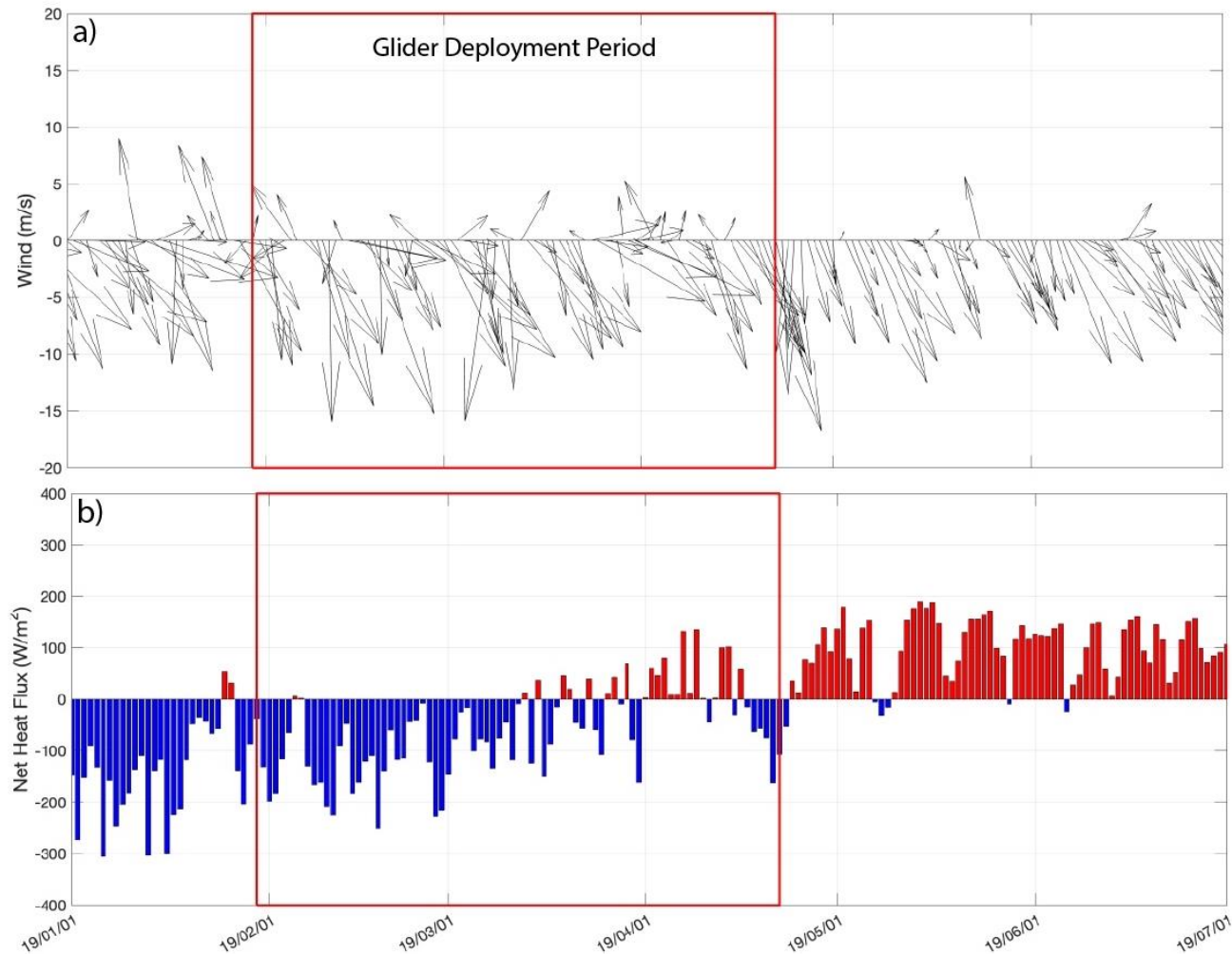
269    **Fig. 2:** a) Wind vectors for the NRS and b) net heat flux for the NRS (average for the black dashed box

270    over the NRS, **Fig. 1**) for the period from January 1, 2019 through July 1, 2019. The red box indicates the

271    period of the glider mission.

272

273    **3.1 Upper ocean response to atmospheric forcing**

274    **3.1.1 Regional response from a remote sensing perspective**

275    Remotely sensed ocean imagery demonstrates the seasonal evolution of the upper ocean during the

276    glider deployment. **Fig. 3** provides images of 8-day composites for SLA and SLA-derived geostrophic

277    velocity, sea surface temperature, and CHL concentration. At the onset of the glider deployment in late

278    January–early February, the eastern boundary coastal flow was northward (**Fig. 3a**). Consistent with this

279    northward flow, a tongue of warmer, low-CHL water extended northward along the Saudi coastline (**Figs.**

280    **3b–c**). These observations are consistent with previous observations from 2016 (Asfahani et al., 2020)

281    and with the mean structure typically observed for SST in the winter months (Karnauskas and Jones,

282    2018). Cooler, higher CHL water is observed on the western side of the basin, perhaps due to the

283    convective mixing described by Kheireddine et al. (2020).

284    Following the initial phase of northward coastal flow, an AE developed in the northeastern RS (**Fig.**

285    **3d**). During this period, the flow was southward across the glider line, and there was no indication of

286    northward advection of warmer, low-CHL water (temperature $> 24°C$ and CHL $< 0.1$ mg/m³) from the

287    south (**Figs. 3e-f**). The AE appeared to block the warmer, low-CHL water transport into the region. The

288    surface temperature of the NRS became cooler reaching a mean surface temperature near 22.5 °C and the

289    temperature difference between the western and eastern sides of the northern region decreased to less than

290    0.25 ˚C (**Figs. 3h** and **4a**).

291    In the latter half of March, two anticyclonic eddies (**Fig. 3g**), between 22 ˚N and 26 ˚N, apparently

292    blocked the northward flow of water from the south and isolated the northern part of the RS from the

293    inflow of the warmer, low-CHL water. Consequently, the near-surface in the NRS became almost

294    thermally homogeneous, with small temperature variations in its spatial distribution (**Fig. 3h**). The densest

295    surface water was observed in the NRS during this period (**Fig. 4c**). By the beginning of April, these two

296    eddies had dissipated, and warm, low CHL water again advected into the NRS along the eastern coastline

297    (**Figs. 3j**, **3k**, and **3l**), re-establishing the temperature differential between the eastern and western halves

298    of the NRS (**Figs. 4a-c**).
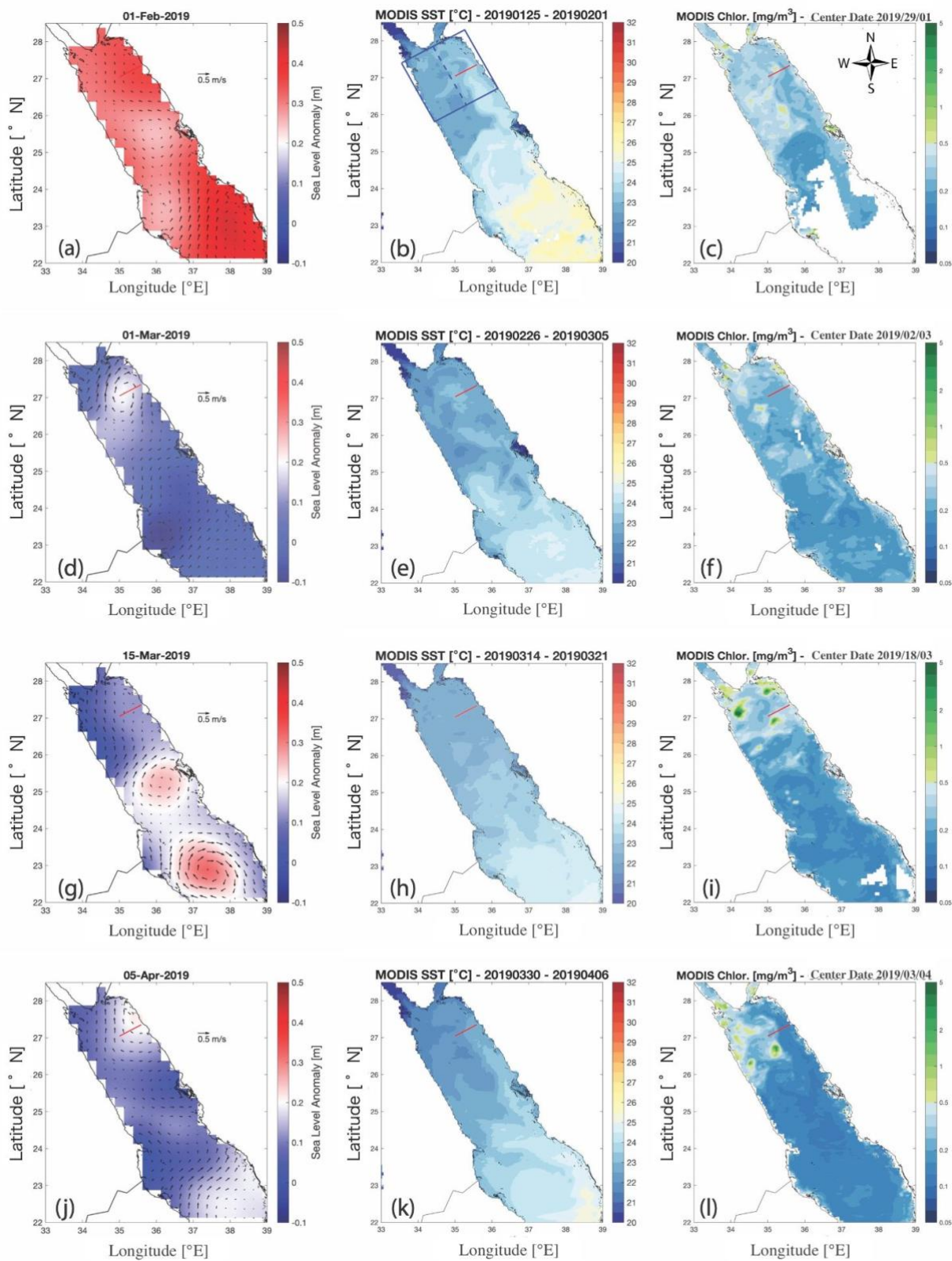
**Fig. 3:** 8-day averages of sea level anomaly and geostrophic velocity (left-hand panels) from AVISO as provided by the Copernicus Marine Environment Monitoring Service (CMEMS), 4 micron nighttime SST from the MODIS Aqua satellite (center panels), and CHL from MODIS OCI (right-hand panels) during the presence of the EBC (panels a-c), AE (panels d-f), pair of anticyclonic eddies (panels g-i), and lateral advection (panels j-l). The red line indicates the location of the Duba glider track. The blue box in panel b) indicates the region of the northern RS (NRS) that was used for regional averages (~ 200 km x 200 km). The dashed blue line divides the eastern half of the NRS from the western half.

### 3.1.2 Upper layer variability

As the atmosphere progressed through its typical annual cycle, the near-surface ocean demonstrated high variability. In order to compare the data accurately, the depth of 6 m has been chosen to represent the near-surface layer, while the depth of 500 m has been selected to represent the near-bottom layer, as it is the most isolated from the surface influence and shows the least variability within the data set. The time series of surface (6 m) and 500 m values for temperature, salinity, and density are shown in **Fig. 4**. This is a continuous time series of glider data, irrespective of its location along the transect. Distinct phases are evident in the time series. The early phase, consistent with the atmospheric forcing, shows a general cooling trend from mixed layer temperatures near 24 ˚C in the early period to about 22.5 ˚C during the coolest phase, after which temperatures rose again to nearly 24 ˚C. For most of the period, the western half of the northern RS was cooler than the eastern half, where the glider was operating (**Fig. 4a**). However, during the coolest period, the temperatures were nearly homogeneous across the entire northern RS. Correspondingly, mixed layer salinities rose from values of 40–40.2 during the early phase to nearly 40.4 during the cool, salty period, then returned to values between 40 and 40.2 in the warming period. As a result, the near-surface density anomaly initially increased from 27.6-27.8 kg/m$^3$ to 28.3-28.4 kg/m$^3$ during the dense period. As expected, no effects of the surface forcing were apparent at 500 m.

In the latter part of the cooling phase (between February 17 and March 12), the MLD exceeded 100 m much of the time. Although the deepest mixed layer occurred during the cool, salty phase, the MLD during this period was highly variable (**Fig. 4d**). The variability in the MLD is a result of the new, well-formed cyclonic eddy during that time. Shallow MLD can be present in the center of a newly-formed cyclonic eddy, as is shown in **Fig. 7**, and it is also consistent with the patchiness of the SST (**Fig. 3e**).

Individual glider sections provide insight regarding mesoscale processes occurring in the NRS during this winter-spring period. In the early cooling phase, the isopycnals were tilted strongly downward from offshore to nearshore, with cool, dense water near the surface offshore and warmer, fresher water near the surface nearshore (**Figs. 5a** and **5b**). The overall geostrophic flow was northward, with an average velocity of 0.31 m/s in the upper 100 m (**Fig. 5e**), consistent with the geostrophic velocity calculated from the sea level anomaly (**Fig. 3a**). The maximum upper layer stratification occurred in the offshore 20 km of the transect, where uplifting of the pycnocline resulted from the cyclonic circulation (**Fig. 5d**). The

335    maximum near-surface CHL concentration occurred where dense water (≥28.1 kg/m3) offshore

336    shallowed to within 50 m of the surface.
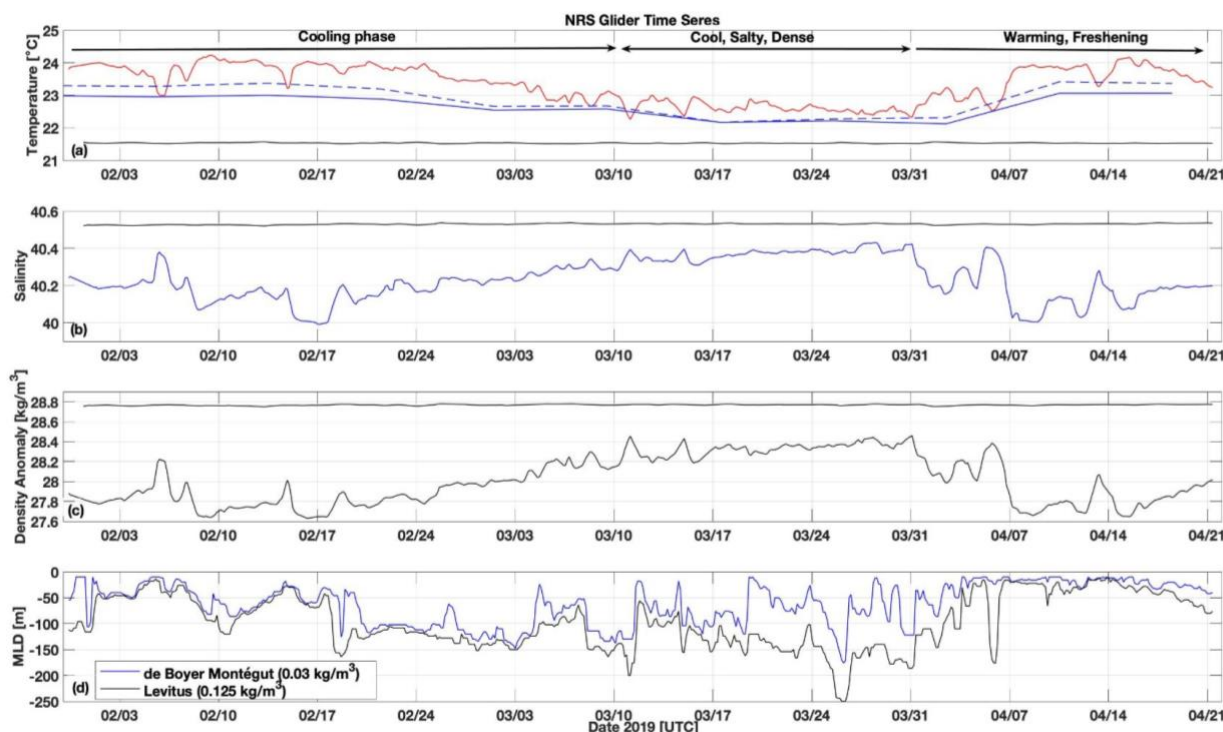


337

338    **Fig. 4:** Time series of near-surface (6 m) and deep (500 m) temperature, salinity, density, and MLD for

339    the glider deployment from January 31 through April 21, 2019. This is the complete time series,

340    irrespective of the glider's location along the transect. In panel a, temperature averages from the 8-day

341    MODIS SST are shown for the entire NRS (solid blue line), the eastern half of the northern RS (NRS-

342    East, dash blue line), and the western NRS (NRS-West, dotted blue line). The geographical boundaries

343    of these subregions are shown in **Fig. 3b**.

344       A small-scale cyclonic feature centered about 43 km offshore was embedded within the larger-scale

345    flow (**Figs. 5a**, **5b**, and **5e**). This feature was not observed in either the previous or subsequent transect,

346    each separated by approximately 3 days from the current transect. Thus, it was a transient feature on the

347    glider line, which we conclude was advected across the glider line within the larger scale flow. A feature

348    characterized by elevated CHL (∼0.03 mg/m³) and DO (∼178 µmol/kg) was observed along the 28.2

isopycnal, between 20 and 40 km offshore, compared to the rest of the transect where CHL was $\sim$0.005 mg/m³ and DO $\sim$94 μmol/kg, respectively, while low BVF is observed in the same area. The feature spanned at a depth range from approximately 150 m at 40 km offshore to 250 m at 20 km offshore, suggestive of subduction of denser near-surface water and downward transport along the isopycnal below the mixed layer and the euphotic zone (**Figs. 5c, 5d, and 5f**). This signal was also present in the backscatter at 650 nm (Fig. 5h). While the higher concentration on the backscatter is evident offshore at the surface ($\sim$4.5 x 10-4 $m^{-1}sr^{-1}$) and decreases with depth and proximity to the shore, in the same area as the elevated CHL and DO, the backscatter reaches values $\sim$3 x 10-4 $m^{-1}sr^{-1}$ , whereas in the surrounding waters it is less than 2 x $10^{-4}$ $m^{-1}sr^{-1}$. This aligns with subduction of CHL (**Fig. 5g)** and backscatter at 650 nm (**Fig. 5h)** along the isopycnals between 28.2-28.3 kg/m$^3$ below the mixed layer and Zeu (120 m) at depths greater than 200 m, contributing to the export of organic matter as it has been observed in other regions of the global ocean (Zarokanellos et al., 2022; Zarokanellos and Jones, 2021; Erickson et al., 2016).

362
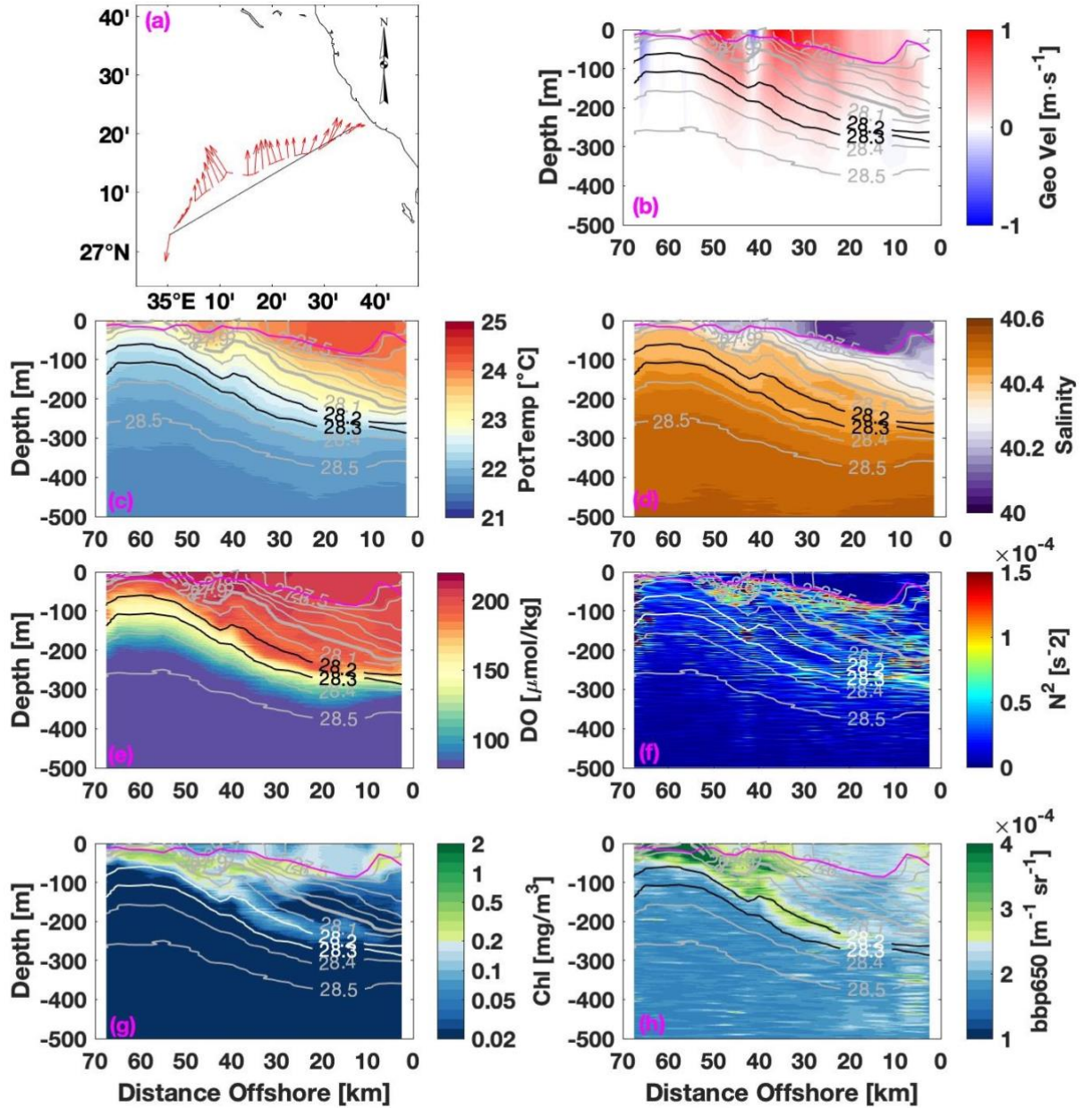
**Fig. 5:** Glider section of a) Depth Averaged Current (DAC), b) Geostrophic velocity, c) Potential temperature, d) Salinity, e) Dissolved Oxygen, f) Brunt-Väisälä frequency, g) Chlorophyll-a, and h) Backscattering coefficient at 650 nm, for February 5–9, 2019. Density isopycnals are shown in subfigures

366   b, c, d, e, f, g, and h with solid grey lines, while the isopycnals of 28.2 and 28.3 are distinguished with

367   black lines (or while for f, g, h). The solid magenta line represents the MLD. Geostrophic velocity,

368   calculated relative to 500 m, is positive to the north-northwest and negative to the south-southeast parallel

369   with the coastline.

370

371       The glider observations of CHL, backscatter at 650, and DO allow us to independently trace the

372   subduction with three different bio-optical tracers. Indeed, the observed elevated CHL is strongly linked

373   to phytoplankton growth, which primarily takes place only offshore within the Zeu, where dense water

374   ($\geq$28.1 kg/m3) rose to a depth shallower than 50 m, bringing up nutrients from deeper layers. Also, the

375   Zeu is located around 120 m in the RS, and light at greater depths is too low to sustain photosynthesis

376   (Zarokanellos and Jones, 2021). Furthermore, this transient eddy about 43 km offshore was not observed

377   in either the previous or the following section, and it was embedded within the larger-scale flow (**Figs.**

378   **5a, 5b, and 5e**). The observed high DO concentration on the surface can be a result of photosynthesis.

379   The co-occurrence of high CHL and DO at depths below the Zeu suggests that this water was originally

380   at the surface before it transferred and subducted deeper. The fact that the high CHL and DO waters align

381   along the 28.2 isopycnal (**Figs. 5, 11a, and 11b**) indicates that their subduction is associated with an eddy

382   wherein the denser surface water is forced below, with the lighter water following the 28.2 isopycnal

383   rather than being vertically mixed

384       Following the initial period of northward transport, the circulation changed significantly in late

385   February, reversing the direction of flow across the glider line due to the presence of an AE in the north-

386   eastern RS (**Figs. 3d-f** and **6**). Based on glider sections, the southward coastal flow began in mid-February

387   and persisted for approximately 3 weeks. The isopycnal structure associated with the anticyclonic

388   geostrophic flow is evident below the mixed layer. In the glider section from March 1–5 the geostrophic

389   velocity varied between weakly northward at the offshore and inshore ends of the line to a maximum

390   southward velocity of 0.67 m/s southward, and an average southward velocity of 0.14 m/s in the upper

391   100m, weaker in magnitude than the northward flow during the preceding cyclonic period (**Fig. 6b**).

392   During this period, the upper boundary of the pycnocline, 28 kg/m3, which had been near the surface

393   offshore during early February, was now at nearly 150 meters depth in the offshore portion of the transect

but rose to the surface near the coast (**Fig. 6**). The MLD was consistently deeper than 100 meters in the offshore 30 km of the transect, and in the near-shore 40 km, it varied between ~25 and 120 m. CHL was uniformly distributed within the mixed layer with diel patterns in concentration, which appear as spatial patterns in the 3.5-day transit of the line (**Fig. 6g**).

Typically, the oxygenated waters are located in the surface layers within the MLD. However, the observed bolus indicated that high oxygenated waters had trapped below the MLD, between the 28.2 and 28.3 kg/m³ isopycnals at 150 to 250 m depths and between 20 and 50 km offshore. The average DO concentration within the bolus is ~177 μmol/kg, while CHL is around 0.0046 mg/m³. The surrounding waters below the 28.3 isopycnal indicate that the DO and CHL values reach 62 μmol/kg and 0.0029 mg/m³, respectively. Above the 28.2 isopycnals, the DO and CHL have values of 203 μmol/kg and 0.079 mg/m³, correspondingly. Compared to the underlying layers, CHL within the bolus is slightly elevated (~3.6%), while DO is significantly higher by approximately 285%. The thickness of the layer between these two isopycnals varies, ranging from less than 40 m, and the thickness of the trapped bolus is approximately 100 m, indicating a distinct water mass that is also associated with low BVF. The observed elevated BVF around the bolus suggests that this is a stable water mass isolated from the surrounding water column rather than a result of vertical mixing. This lens is slightly warmer (~22.3°C) and more saline (~40.43) than other waters within the same isopycnal range along the transect (**Fig. 6c, 6d, 6f**). While its signature was not reflected in CHL (**Fig. 6g**), the bolus is also detectable in backscatter (**Fig. 6h**), with a concentration nearly 11% higher than the surrounding waters (**Fig. 6h**). This bolus is likely outflow water from the Gulf of Aqaba, which might be advected into the region by the southward flow and subsequently captured and recirculated by the observed AE (**Fig. 6a**). Only a few studies are available regarding the water mass characteristics of the Gulf of Aqaba (Manasrah, 2002; Manasrah et al., 2004), suggesting that the upper 300 m of the Gulf exhibit conditions similar to those found in the upper 100 m of the NRS during winter, with temperatures ranging from 20.4°C to 22.4°C and for the salinity between 40.3 and 40.7.

The near-surface temperature continued to decrease through March, while salinity increased within the surface layer, reaching a maximum salinity of 40.4 and a density anomaly of about 28.4 kg/m³ in late March (**Fig. 4**). The corresponding glider section of temperature and salinity for this period (**Figs. 7c-d**),

422  March 26–29, shows that the coolest, saltiest, and densest water occurred in the center of a cyclonic eddy

423  about 40–45 km offshore, where the dense isopycnals (>28.2 kg/m$^3$) outcrop at the surface. Across this

424  transect, the near-surface temperature was less than 22.8 ˚C, the minimum salinity was more than 40.3,

425  the minimum near-surface density was >28 kg/m$^3$, and the minimum stratification was <1x10$^{-4}$ (**Fig. 7f**).

426  Prior to this, the shallowest that the 28.2 kg/m$^3$ isopycnal was observed was in the early section between

427  February 5 and 9, at a depth of about 90 m at the offshore end of the transect. In the same transect, the

428  isopycnal descended below 250 m nearshore. Mixed layer depth along this transect ranged from as

429  shallow as 12 m to as deep as 148 m on the inshore end of the transect, on the periphery of the eddy

430  circulation. In the eddy center, the mixed layer extended to the depth of the 28.3 kg/m$^3$ isopycnal where

431  stratification due to the uplifted pycnocline impeded deeper mixing. The isopycnal uplifting appears to

432  be in the center of a cyclonic feature where the geostrophic velocity (**Fig. 7a, 7b**) is northward nearshore

433  (0.5 m/s) and southward offshore (0.2 m/s).

434
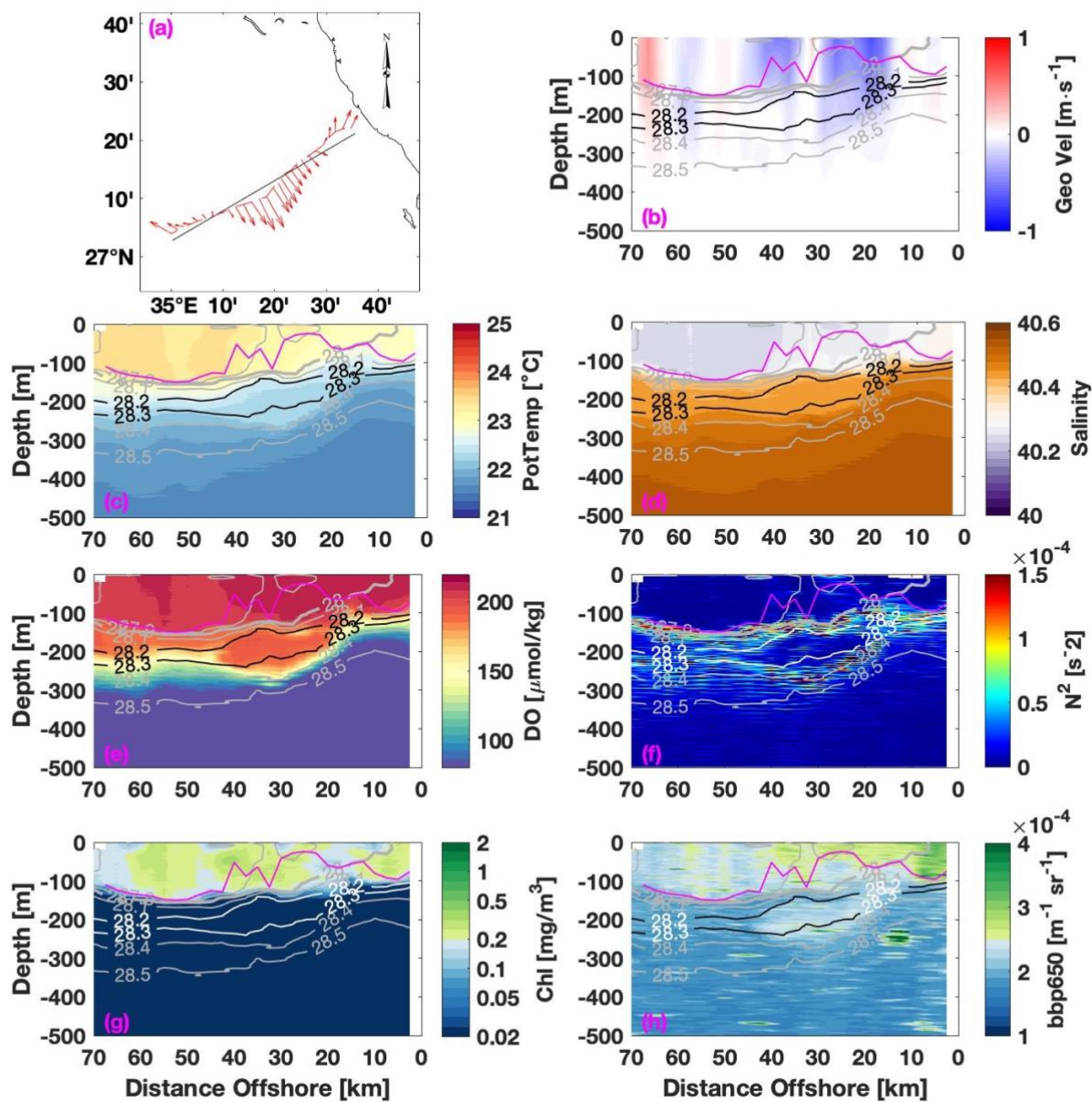
**Fig. 6:** Same as for **Fig. 5**, but for the period of March 1–5, 2019

26

As in earlier sections, small-scale structures are apparent and potentially important to biogeochemical processes. At about 20 km offshore, a low DO and low CHL feature extends upward from about 200 m to at least 100 m depth (**Figs. 7e-g**). The low DO concentration extends to shallower depths. The uplift of isopycnals affects the biogeochemical processes by bringing low DO and CHL waters into the Zeu. This process modulates nutrient, carbon, and DO availability and ultimately affects primary production. Phytoplankton growth depends on the nutrients and light availability. The low-CHL waters typically indicate nutrient-depleted conditions at the surface, while the low-DO waters in deeper layers are generally enriched with remineralized nutrients such as nitrate, phosphate, and silicate (Garcia H.E. et al., 2018). In this case, the low-CHL and DO waters have reached ～60 m, penetrating the Zeu, which extends to ～120 m, as reported by Zarokanellos and Jones (2021). When these nutrient-available waters reach the Zeu, they can stimulate phytoplankton blooms, enhancing primary production (Falkowski et al., 1998). Further, the uplift of the 28.3 isopycnal (～60 m) due to the presence of the cyclonic eddy (**Fig. 7**) affects nutrient availability (Zarokanellos & Jones, 2021; Kurten et al., 2019). This mesoscale eddy activity in the region often drives the shift in the phytoplankton community (Kurten et al., 2019).

The presence of the CE leads to an uplift of the isopycnals about 50 km offshore (**Fig. 7**). In the shoreward periphery of this eddy (~20 km offshore), both CHL and DO penetrate to a depth of up to 250 m, well below the mixed layer and the Zeu depth (**Figs. 7g** and **7e**). This subduction occurs near the nearshore reversal of flow. Unfortunately, no backscatter data were acquired during this period (**Fig. 7h**).
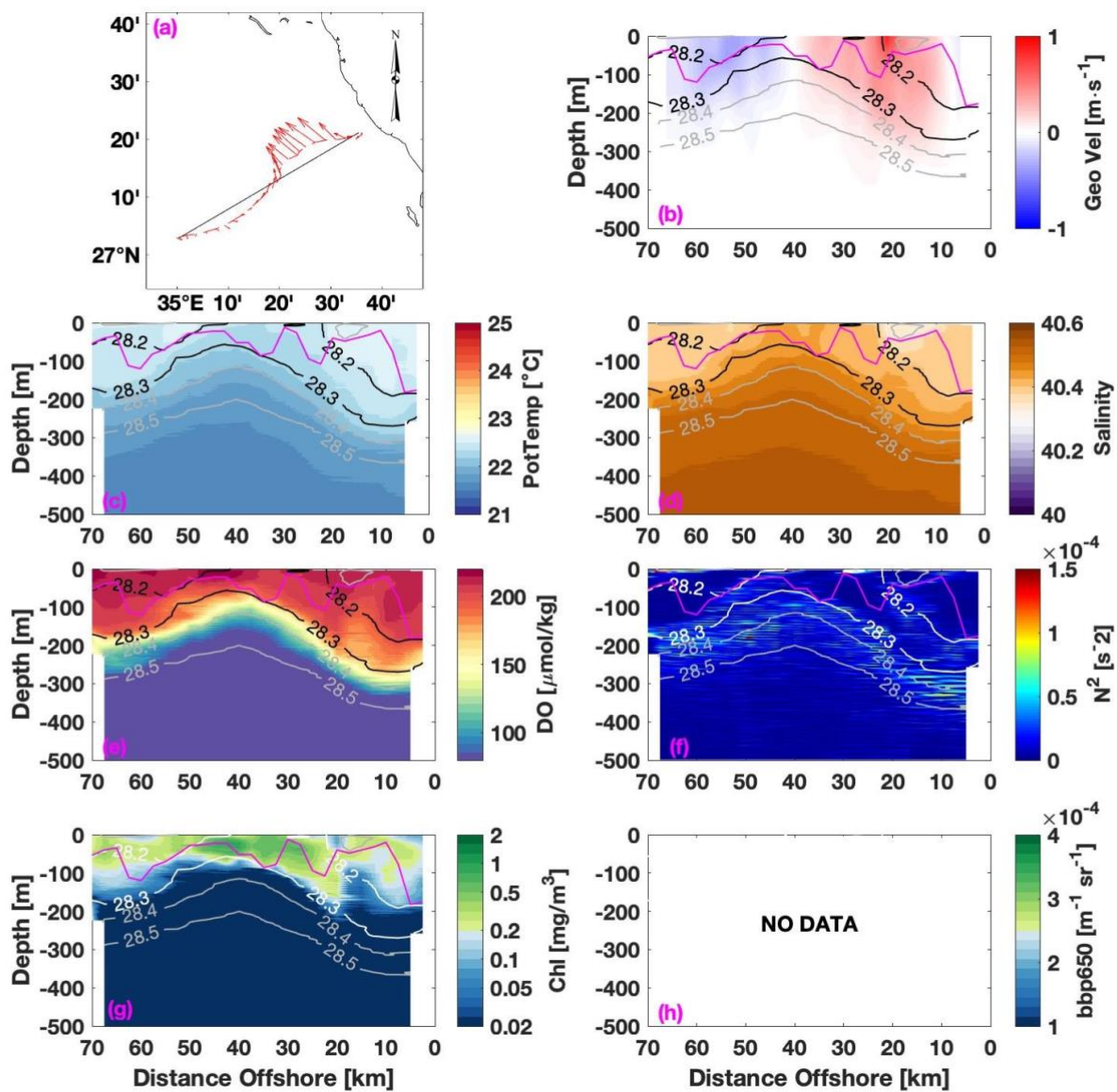
454

455

**Fig. 7:** Same as for **Fig. 5**, but for the period of March 26–29, 2019.

457

458    Immediately following this cool period, warmer, fresher water began to appear in the nearshore region

459    of the glider line (**Figs. 8c-d**). The shallowing of lower-oxygen water, hence nutrient-rich, offshore

460    between 35 and 50 km was observed in late March and subsided with the weakening of the cyclonic

461    circulation (**Fig. 8e**). The cyclonic circulation remained (**Fig. 8a**), but it was entraining the warmer,

462    fresher water from the south, as is evident in the composite SST image from March 30-April 6 (**Fig. 3k**).

463    This warming and freshening continued through the remainder of the glider deployment (**Fig. 4a**).

464    Freshening was evident on the nearshore half of the glider line, where salinities fell below 40.3, while

465    remaining higher along the offshore half of the line. Denser water subsided except at the outer half of the

466    transect. Although the direction of the geostrophic velocity was similar in pattern to the previous period

467    (**Fig. 7e**), the magnitude of the nearshore flow intensified by 0.2 m/s, while the offshore flow was similar

468    to the previous transect (**Fig. 8b**). **Fig. 8g** shows that the CHL concentration between 35 and 50 km

469    offshore decreased as warmer water was entrained near the coast.

470    Subduction is also present between 30 and 10 km onshore and is clearly observed in the BVF panel

471    and in CHL and DO (**Figs. 8b, 8e,** and **8g**). The subduction displaces the pigments of CHL and DO deeper

472    than 200 m nearshore; in the offshore area, these two parameters are well distributed in the first 100 m.

473

474
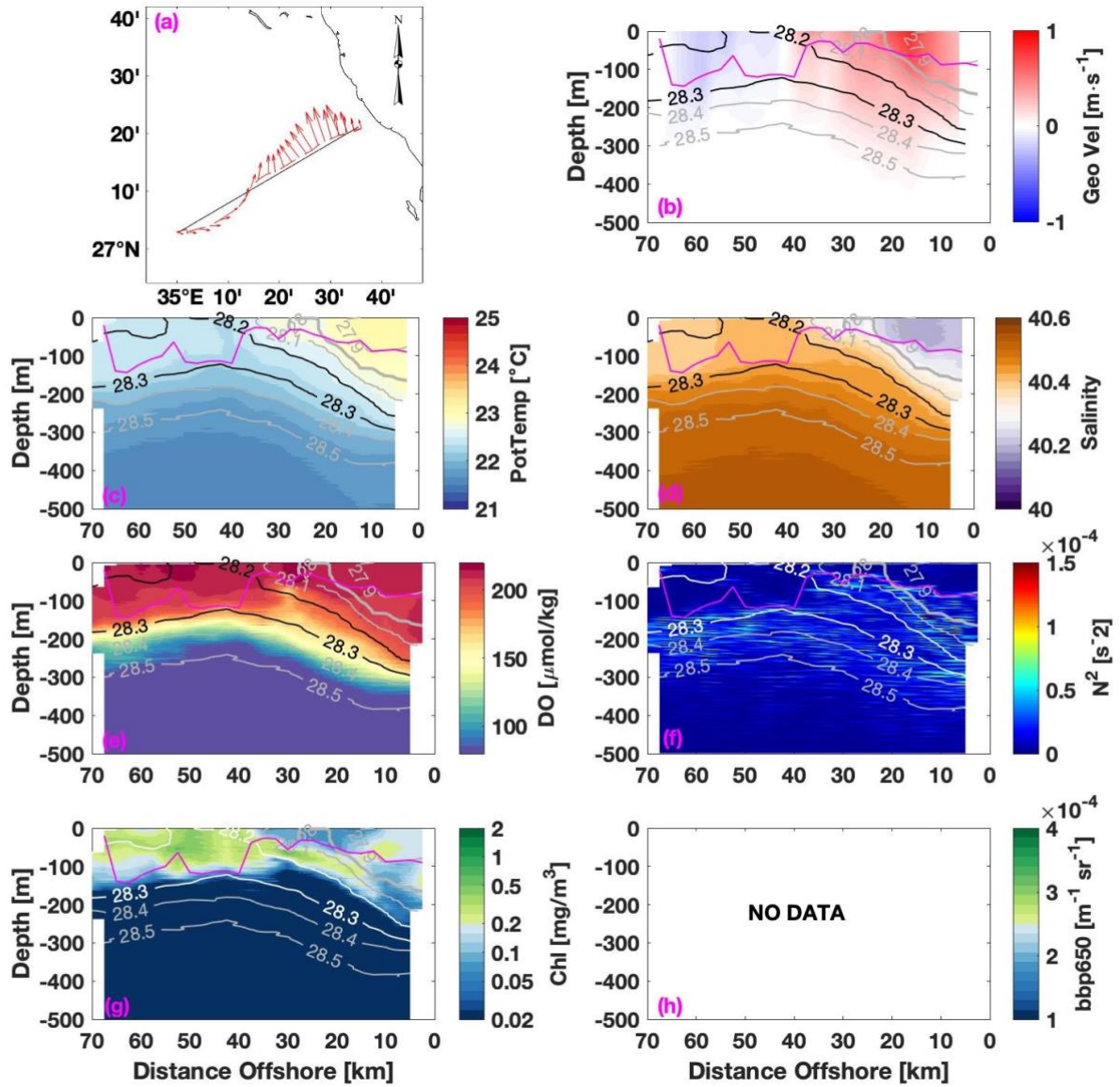
**Fig. 8:** Same as for **Fig. 5**, but for the period of March 29-April 2, 2019.

## 4. Discussion

The NRS is a dynamic and complex three-dimensional circulation with significant seasonal variability influenced by strong atmospheric forcing through wind stress and air-sea buoyancy fluxes. Direct  observations and modeling experiments have both captured the formation of locally produced intermediate (RSOW) and deep water (RSDW) masses and their interactions with adjacent gulfs of Suez and Aqaba (Table 2; Asfahani et al., 2020; Sofianos and Johns, 2003; Papadopoulos et al., 2015). Two main thermohaline cells are associated with water mass formation and influenced by mesoscale dynamics, wintertime cooling, and deep convection. Numerical simulation studies suggest that the cyclonic gyre is the most probable site for RSOW formation (Yao et al., 2014a; Sofianos and Johns, 2003).

Unlike previous observations and interpretations of the NRS (e.g., Asfahani et al., 2020; Papadopoulos et al., 2015; Yao and Hoteit, 2018), a reversal of the currents in the eastern half of the basin prevented the inflow of warmer, fresher water from the south. During this phase, the upper layer of the NRS became relatively homogeneous, and near-surface water along the glider line reached its maximum salinities and densities (**Figs. 5d** and **7d**).

To evaluate the similarities and differences with previous years, an EOF analysis was performed on the SLA data between 26 ˚N and 28 ˚N over a period of 4 years that has been considered efficient (from 2016 to 2019; **Fig. 9**). The first mode of the EOF describes 86.6 % of the SLA variation (**Fig. 9a**). In the years 2016–2018, the EOF of the SLA showed a relatively positive or neutral pattern during the winter-spring transition period, which continued until May, when the EOFs typically decreased (**Fig. 9b**). This late spring decrease generally coincides with the transition from a net negative air-sea heat flux to a net positive flux (see **Fig. 2b**). For 2019, the first mode of the EOF showed a distinct increase in late January through mid-February, then became negative through mid-March, in contrast to the pattern in previous years.  This negative phase is consistent with the period when the circulation was anticyclonic (**Fig. 9b**). The flow of warmer, fresher water from the south was apparently blocked during this period, and the temperature became relatively homogeneous in the NRS, as have been previously observed in the CRS (Zarokanellos et. al., 2017). Recently, a study by Mohamed and Skliris (2025) showed that the annual climatology of the sea level is generally higher on the eastern boundary of the RS compared with the western boundary, where many areas are isolated patches of higher or lower values of SLA indicate

504 mesoscale activity. The maximum values correspond with regions where AEs are present. In our study,
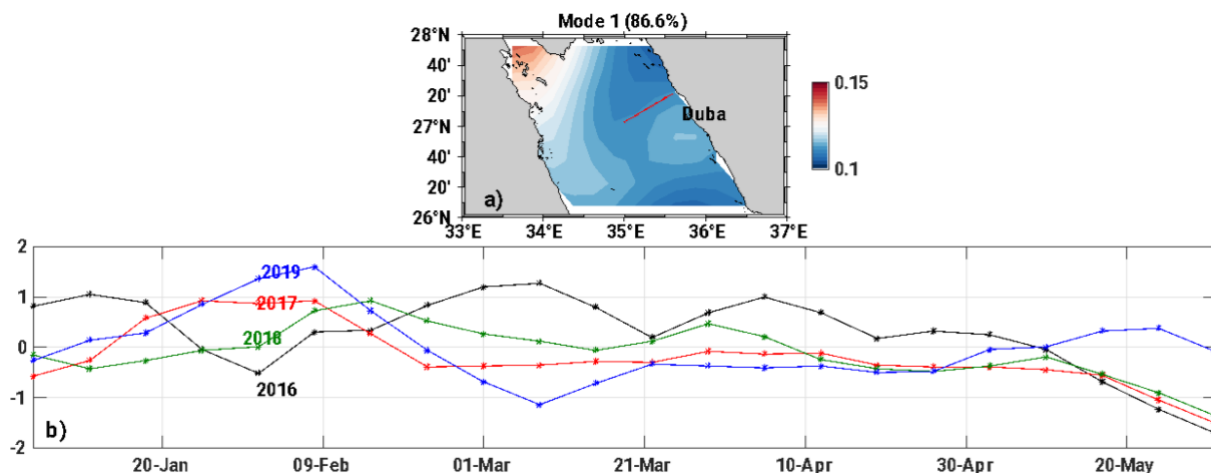505 the negative phase of the EOF analysis (**Fig. 9b**) aligns with the presence of AE in the NRS.



506

507 **Fig. 9:** The first mode of the EOF based on the SLA weekly mean in 2019. (a) the spatial pattern of the
508 first mode. (b) time series graph of the first mode for four (4) subsequent years: 2016 (black), 2017 (red),
509 2018 (green), and 2019 (blue) from January to May.

510     We examined the relationship between the first mode of the EOF and atmospheric forcing using a
511 time-lagged correlation. No clear correlation was discernible from this analysis (not shown). But in
512 comparison with the previously published observations from 2016 (Asfahani et al., 2020*)*, the period of
513 negative average heat flux lasted longer into the spring. Thus, there is an overall difference in the duration
514 of the negative heat flux between the 2016 observations and the observations in 2019.

515     The surface layers responded to the heat loss with decreased temperatures and increased salinity and
516 density. The cumulative effect of the cooling through the entire winter period resulted in the formation of
517 the densest surface waters in late March, when the difference in temperature and salinity between the
518 surface and the deep layers was at a minimum. Following this cooling phase, the net heat flux fluctuated
519 around zero. Then in early April, the weakening of the atmospheric forcing, the transition to positive heat
520 fluxes, and restratification due to advection from the south resulted in a near-surface temperature increase
521 of 1°C and a salinity decrease of 0.2, both of which contributed to the near-surface density decrease in
522 April (**Fig. 4**). The warmer, less saline, and thus lighter water from the south spread into the area, and

during the restratification, it overrode the denser waters, isolating them from additional direct ocean-atmospheric interaction.

The water underlying the more buoyant surface water, which lies along the 28.2 kg/m$^3$ isopycnal, extended from the surface in mid-transect to approximately 200m nearest the coast (**Fig. 8**). This recently exposed subsurface water spreads in the basin, and its signal can be detected in the CRS, as mentioned by Zarokanellos and Jones (2021). This water results from the northward advection of GASW, which is subjected to evaporation along its entire transit of the RS. Winter cooling throughout the entire period further modifies the transported surface water in the NRS. During this particular year, the presence of the AE in the NRS temporarily blocked advection from the south, contributing to the surface waters' extended exposure to the atmosphere. Near the end of the cooling period, when the surface water reached its maximum density, the cyclonic circulation was reestablished, contributing to the inflow of buoyant GASW which overlaid the denser water.

In this study, the PWP model was applied to subsets of the observational period to further understand the relationship between the local heat flux and the advection of water from the south. The PWP model used daily surface heat flux and wind stress, as a pronounced diurnal cycle was not evident in the observed salinity and temperature data. While this simple 1-dimensional model cannot capture the spatial variability of the water column structure or the atmospheric forcing field, it effectively illustrates the role of atmospheric forcing in driving the seasonal evolution of the mixed layer in the absence of these complexities. In contrast, Krokos et al. (2022) used a 4-dimensional MIT-GCM model to investigate the spatial and seasonal evolution of mixed layer variability across the entire RS, highlighting the critical role of atmospheric forcing, particularly through its influence on mixed layer temperature. This broader modeling approach supports the atmospheric-driven dynamics demonstrated by our PWP findings.

**Fig. 10** shows the evolution of the MLD in the upper 200 m based on the PWP simulation. Three separate PWP simulations were performed, initiating each simulation at the onset of one of the three phases determined from the in-situ observations. The initial temperature and salinity profiles for the model run were taken from the glider section nearest the initiation point of the run. The cooling phase extended from February 1st until March 8th (35 days). During this period, first presence of a mesoscale cyclonic

eddy and later an anticyclonic eddy in the study area were observed. In the same period, the simulated MLD is constantly deepening, reaching a maximum depth of 162m at the end of the cooling phase.

During the dense phase, the observed MLD shows large fluctuations and mismatches with the simulated MLD. The 1-D model failed to capture the shallowing of MLD during the dense phase. The observed discrepancy is based on the pycnocline depth that shallowed substantially, such that the dense pycnocline intersected with the surface. Lastly, the PWP-simulated MLD during the warming phase also shows a discrepancy with the observed MLD. During this phase, the observed MLD rapidly shallowed to less than 45 m, and the mean MLD was about 20 m. The shallowing of the MLD during the warming and freshening phases was attributed, in part, to the northward flux of the buoyant Gulf of Aden Water. But the shallowing of the pycnocline due to the cyclonic eddy also contributed to the shallowing of the MLD, as seen clearly in **Fig. 8**. In addition, the shallowing of the MLD due to the presence of the CE facilitates exporting the surface water masses to the deeper layers below the euphotic zone, as indicated from the backscatter (**Fig. 5 h**).
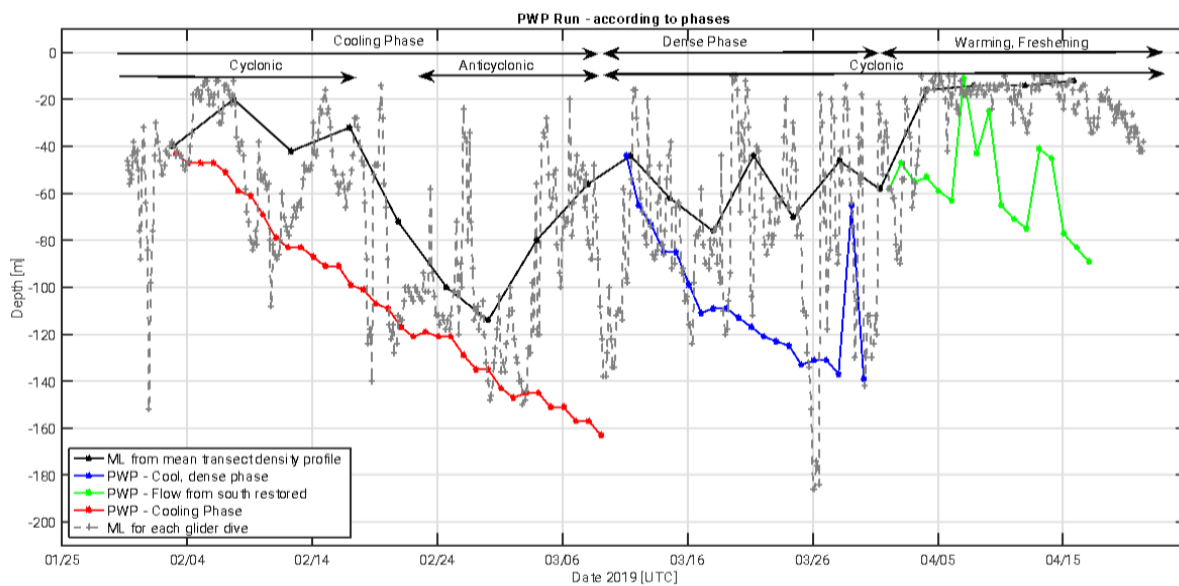


**Fig. 10:** Comparison between the observed transect-averaged MLD from the glider (black) and PWP-simulated MLD during the 1) cooling phase (red), 2) cool-salty and dense phase (blue), and 3) warming-freshening phase (green). The black + symbol shows the MLD for each dive, interconnected by the black dashed line.

568

569      Water mass subduction along isopycnals is a component of the formation of RSOW during winter

570    and a contributor to the carbon flux from the Zeu to the interior of the RS. As shown in **Fig. 5**, a water

571    mass containing elevated CHL and DO can extend well below the mixed layer and Zeu. Although only

572    one example with this feature (February 5-9, **Fig. 5**) is shown in this paper. Subducted water was evident

573    in the glider deployment from its deployment on January 30 through the fourth transect that was

574    completed on February 18. Key characteristics of this feature were elevated CHL and DO on the 28.2

575    $kg/m^3$ isopycnal that extended to as deep as 250 meters. In **Fig. 5**, this feature was evident from about 45

576    km offshore and shoreward. **Fig. 11** shows the relationship between these variables and density between

577    20 and 40 km offshore. A clear peak in both variables aligns with the 28.2 $kg/m^3$ isopycnal. Inshore, at

578    45 km, the region between 150 and 500 m contains a measurable fraction of the total CHL. In addition,

579    **Fig. 11d** shows that the subduction event contributes 20% to the integrated CHL between 150 and 500m.
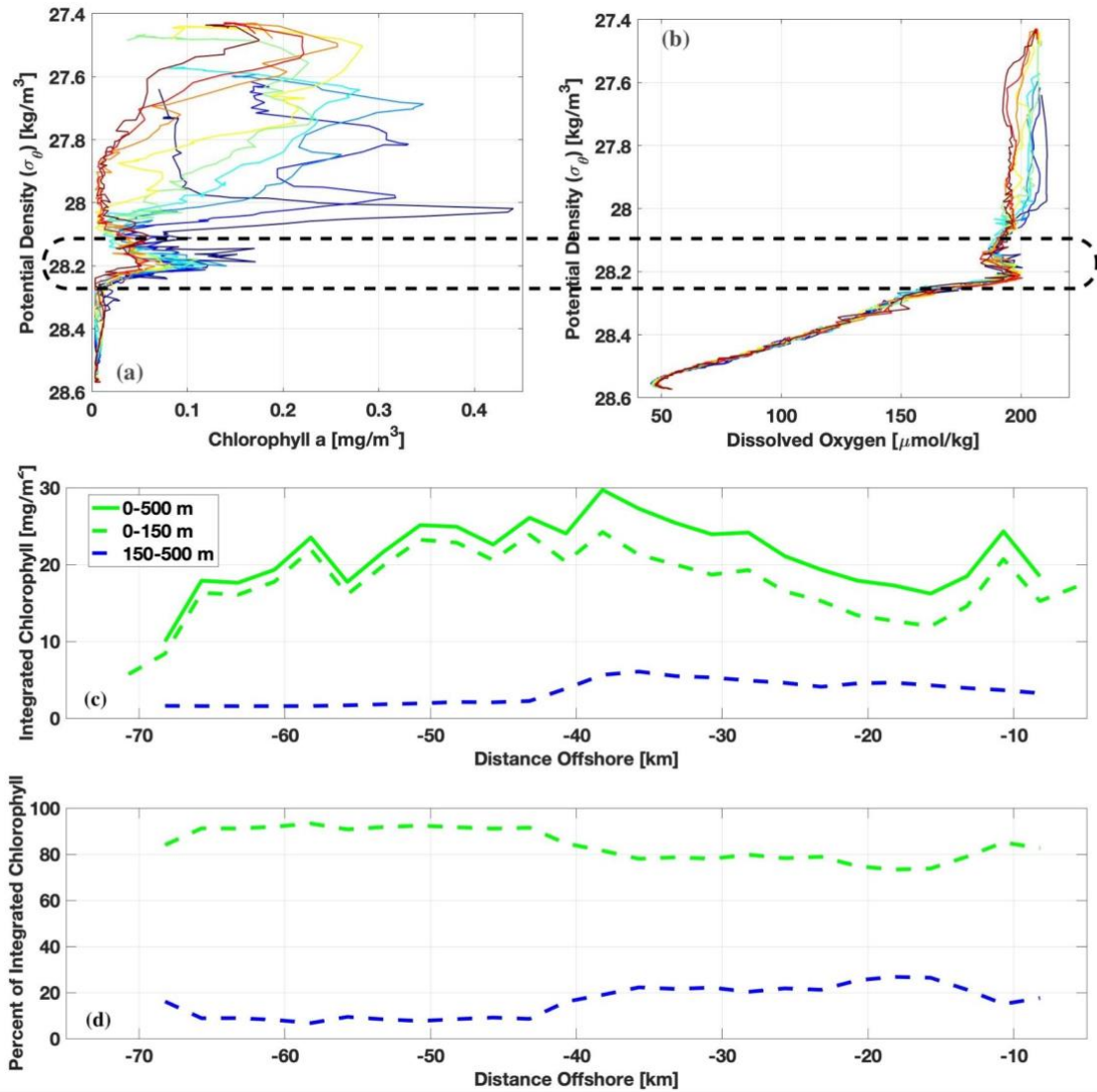
580



581

**Fig. 11:** Characteristics of the subducted feature in transect 2, February 4–9 (**Fig. 5**). Panels a and b show the concentrations of chlorophyll and dissolved oxygen as a function of density for profiles between 20 and 40 km offshore. Panel c shows the integrated chlorophyll as a function of distance offshore The solid green line is the total integrated chlorophyll between the surface and 500 meters. The dashed green line is the integrated chlorophyll between the surface and 150 m, and the blue line is the integrated chlorophyll between 150 and 500 m. Panel d shows the percentage of the integrated chlorophyll from 0 to 150m (dashed green line) and from 150 to 500m (dashed blue line).

36

Given the limitations of our observations, constrained by the Exclusive Economic Zone (EEZ) boundary, the full mechanism of the formation of this subducted layer is unclear. One possible mechanism is that either vertical mixing or sinking of particles on the western half of the NRS (Kheireddine et al., 2020) could create this feature, which is then entrained into the cyclonic circulation in this region and transported from the western side of the basin to the eastern side. **Fig. 12** shows a conceptual diagram of RSOW subduction and its biogeochemical impact on the NRS based on the existing observations. Regardless of the details of the mechanism, subduction is a process that needs to be considered in the physical and biogeochemical dynamics of the NRS.
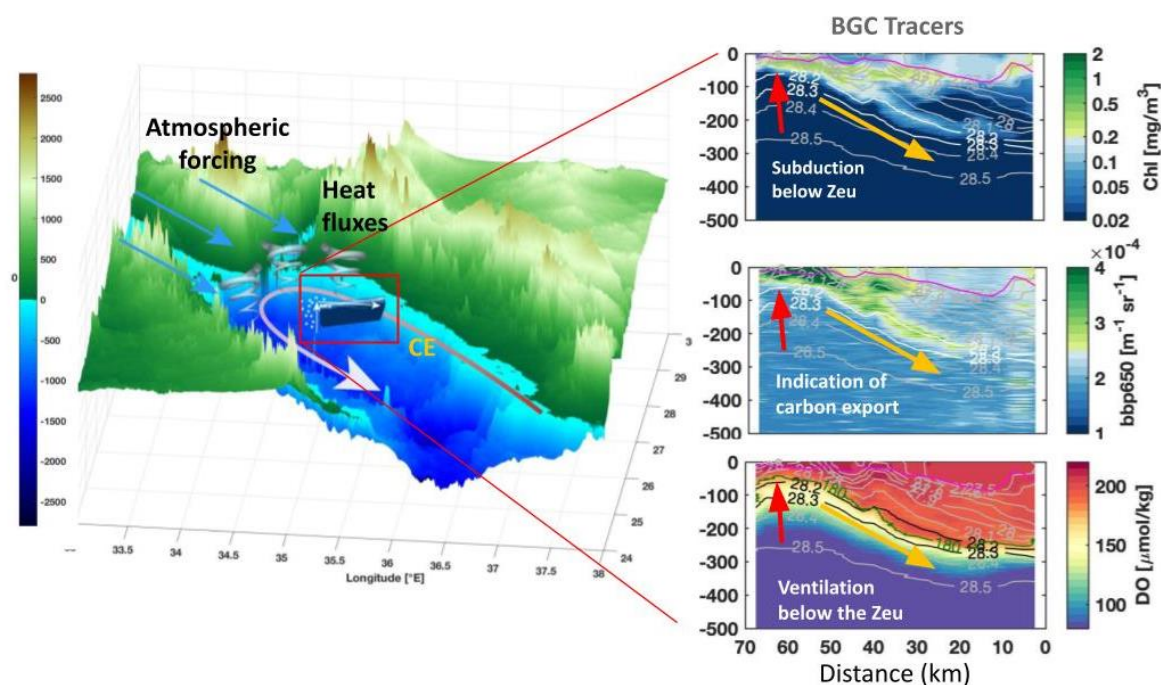


**Fig. 12:** Conceptual diagram of RSOW subduction and its biogeochemical impact on the NRS. Topographic and bathymetric representation of the study area where physical and atmospheric processes superimposed on the map indicate the general cyclonic circulation (grey arrow), the influence of atmospheric forcing (blue arrows), and heat fluxes (grey spirals; left panel). Panels on the right display

604    the glider section of CHL (top), backscatter at 650 nm (middle), and DO (bottom). Red rows correspond

605    to the uplifting of the isopycnal and yellow arrows to the subduction of the newly formed RSOW.

606    Subducted CHL, backscatter at 650 nm, and DO are traced below the Zeu (~120 m) associated with carbon

607    export and ventilation of the deeper layers. The green isopleth of 180 μmol/kg presents the nitracline

608    (bottom-right panel).

## 5. Conclusion

The primary objective of this study was to understand the mechanisms contributing to the water mass formation of RSOW in the NRS and the associated biogeochemical responses. Our findings demonstrate that the RSOW formation is closely linked to the presence of a cyclonic eddy and intense winter cooling, consistent with previous studies (Asfahani et al., 2020; Sofianos and Johns, 2003; Papadopoulos et al., 2015; Yao et al., 2014b). A novel finding of this study is the role of water mass subduction, which, although not previously discussed, contributes not only to the RSOW formation but also to the carbon export as CHL and backscatter indicated that water has been subducted below the Zeu (**Fig. 12**). The observations also indicate that subduction events can significantly contribute to the ventilation of intermediate and deeper waters, thereby affecting the overall oxygen budget of the RS. During these events, oxygen-rich surface waters are transported into subsurface layers along the 28.2 kg/m³ isopycnal, facilitating oxygen redistribution at depth. The study also identified a transition from negative to positive heat flux and the re-establishment of northward flow along the eastern RS coast, signalling the cessation of the RSOW formation as less dense water from the south caps the denser northern waters. The presence of the AE south of the study area prevented the advection of more buoyant surface water. Although we could not determine the mechanism for this reversal of CE to AE from our observations and 1D model simulations. This likely influenced the observed water mass originating from the northern gulfs within the RSOW density range, consistent with Papadopoulos et al. (2015). This study highlights that multiple factors can contribute to RSOW formation (**Table 2**), including dense isopycnal surfacing from cyclonic circulation, vertical mixing, dense outflow from the northern gulfs, water mass subduction, the extension of dense isopycnal exposure due to blockage of buoyant flux from the south, and the eventual termination of these processes as the buoyancy flux is restored. In addition, it is clear that the submesoscale features are present in the region and contribute to the overall physical and biogeochemical dynamics of the region. To comprehensively capture the spatial and temporal dynamics of RSOW formation, future research should prioritize detailed observational and modeling studies, integrating autonomous platforms and ship-based sampling across the entire NRS basin. Such an approach would resolve the three-dimensional variability and provide valuable insights into the sources and sinks involved in RSOW formation and its biogeochemical impacts.

| Contributing Mechanisms | Yao et al 2014 (a & b) | Papadopoulos et al 2015 | Asfahani et al 2021 | Krokos et al 2022 | This Study |
|---|---|---|---|---|---|
| Cyclonic Circulation leading to exposure of dense isopycnals | √ | √ | √ | | √ |
| Convective mixing | √ | √ | √ | √ | √ |
| Upwelling/Downwelling along boundaries | √ | | | | |
| Outflow from Gulfs | | √ | | | √ |
| Along basin pressure gradients | √ | | | | |
| Submesoscale processes | | | | | √ |
| Subduction of dense water from surface water into pycnocline | | | | | √ |
| Anticyclonic blockage of northward flow of buoyant water into NRS | | | | | √ |
| **Biogeochemical effects** | | | | | |
| Eddy driven upwelling nutrient flux | | √ | √ | | √ |
| Convective mixing nutrient flux into euphotic zone | | | √ | | √ |
| Subduction results in the downward transport of dissolved oxygen and | | | | | √ |

| particulate carbon below the euphotic zone | | | | | |
|---|---|---|---|---|---|
| | | | | | |

638

639 **Table 2:** Summary of the major conclusions from the related studies relative to the formation of the
640 RSOW in NRS.

**Data availability**

The data sets that are presented in this paper (glider time series and gridded sections, 8-day remotely sensed SST, chlorophyll, and sea level anomaly/geostrophic velocity, and the NASA MERRA-2 reanalysis data) are available through the Zenodo repository (https://doi.org/10.5281/zenodo.11046900) https://zenodo.org/records/11046900?preview=1&token=eyJhbGciOiJIUzUxMiJ9.eyJpZCI6IjA4Z DdkMzY0LTQyMGUtNGRiYS1iYTVmLWRkYjhlM2M2M2I2YyIsImRhdGEiOnt9LCJyYW5kb20iO iI2MWM1YjUyOGQxZDBkYmRkOTc5MjI4MDYxZWEwMGJlZCJ9.VHVgGkzDwCZ1576vzMKco mKl4Zax-uy9lbG_XHE1zfT_ag31O5DHNh0VHlJDWQNxfrn0S3HBbOXS_2QhoPTbDQ.

**Author contribution:**

All authors have contributed to Conceptualization, Data Curation, Formal Analysis, Investigation, Writing – original draft preparation and Writing – review & editing. Visualization is done by L.E., Z.K. and B.H.J.. Software is done by L.E. and B.H.J.. while supervision is done by Z.K. and B.H.J.

**Competing interests**

The authors declare that they have no conflict of interest.

**References**

Abualnaja, Y., V. P. Papadopoulos, S. a. Josey, I. Hoteit, H. Kontoyiannis, and D. E.: Raitsos Impacts of Climate Modes on Air-Sea Heat Exchange in the Red Sea, Journal of Climate, 28(7), 2665–2681, doi: 10.1175/JCLI-D-14-00379.1, 2015.

Asfahani, K., G. Krokos, V. P. Papadopoulos, B. H. Jones, S. Sofianos, M. Kheireddine, and I. Hoteit: Capturing a Mode of Intermediate Water Formation in the Red Sea, Journal of Geophysical Research: Oceans, 125(4), e2019JC015803, https://doi.org/10.1029/2019jc015803, 2020.

Al Senafi, F.; Anis, A.; Menezes, V. Surface Heat Fluxes over the Northern Arabian Gulf and the Northern Red Sea: Evaluation of ECMWF-ERA5 and NASA-MERRA2 Reanalyses. *Atmosphere*, *10*, 504. https://doi.org/10.3390/atmos10090504, 2019.

Beal, L. M., A. Ffield, and A. L. Gordon: Spreading of Red Sea overflow waters in the Indian Ocean, Journal of Geophysical Research, 105(C4), 8549–8564, doi:10.1029/1999JC900306, 2000.

Biton, H. Gildor, and W. R. Peltier: Red Sea during the Last Glacial Maximum: Implications for sea level reconstruction, Paleoceanography, 23, PA1214.doi:10.1029/2007PA001431, 2008.

695　　　Biton, Gildor, Trommer, Siccha, Kucera, van der Meer, and Schouten: Sensitivity of Red Sea
696　　circulation to monsoonal variability during the Holocene: An integrated data and modelling study,
697　　Paleoceanography, 25(PA4209), 1-16, doi:10.1029/2009PA001876, 2010.

698　　　Bower, A. S., and J. T. Farrar: Air-Sea Interaction and Horizontal Circulation in the Red Sea, in The
699　　Red Sea, edited by N. M. A. Rasul and I. C. F. Stewart, pp. 329-342, doi:10.1007/978-3-662-45201-1_19,
700　　2015.

701　　　Bower, A. S., and H. H. Furey: Mesoscale eddies in the Gulf of Aden and their impact on the spreading
702　　of Red Sea Outflow Water, Progress in Oceanography, 96(1), 14-39, doi:10.1016/j.pocean.2011.09.003,
703　　2010.

704　　　Cember, R. P.: On the sources, formation, and circulation of Red Sea deep water, Journal of
705　　Geophysical Research: Oceans, 93(C7), 8175-8191, doi:10.1029/JC093iC07p08175,1988.

706　　　Chen, C., Li, R., Pratt, L., Limeburner, R., Beardsley, R. C., Bower, A., Jiang, H., Abualnaja, Y., Xu,
707　　Q., Lin, H., Liu, X., Lan, J., & Kim, T.: Process modeling studies of physical mechanisms of the formation
708　　of an anticyclonic eddy in the central Red Sea, Journal of Geophysical Research: Oceans, 119, 1445–
709　　1464. doi:10.1002/2013JC00935, 2014

710　　　Churchill, J. H., Lentz, S. J., Farrar, J. T., Abualnaja, Y.: Properties of Red Sea coastal currents,
711　　Continental Shelf Research, 78, 51–61.doi:10.1016/j.csr.2014.01.025, 2014.

712　　　　Clifford, M., C. Horton, J. Schmitz, and L. H. Kantha: An oceanographic nowcast/forecast system
713　　for the Red Sea, Journal of Geophysical Research, 102(C11), 25,101-125,112. doi:  10.1029/97JC01919,
714　　1997.

715　　　de Boyer Montegùt, C., G. Madec, A. S. Fischer, A. Lazar, and D. Iudicon: Mixed layer depth over
716　　the global ocean: An examination of profile data and a profile-based climatology, Journal of Geophysical
717　　Research, 109(C12003), doi:10.1029/2004JC002378, 2004.

718　　　Edwards, A. J., and S. M. Head: Red Sea, Key Environments Series, Pergamon Press, Oxford,
719　　doi:10.1016/B978-0-08-028873-4.50008-6, 1987.

720　　　Emery, W. J.: Water types and water masses, in Encyclopedia of ocean sciences, edited, pp. 3179-
721　　3187, Elsevier, doi: 10.1006/rwos.2001.0108, 2001.

722 Erickson, Z. K., A. F. Thompson, N. Cassar, J. Sprintall, and M. R. Mazloff , An advective mechanism
723 for deep chlorophyll maxima formation in southern Drake Passage, *Geophys. Res. Lett.*, 43, 10,846–
724 10,855, doi:10.1002/2016GL070565, 2016.

725 Eshel, M. A. Cane, and M. B. Blumenthal: Modes of subsurface, intermediate and deep-water renewal
726 in the Red-Sea, Journal of Geophysical Research: Oceans, 99(C8), 15941-15952. doi:
727 10.1029/94JC01131, 1994.

728 Eshel, and N. H. Naik: Climatological Coastal Jet Collision, Intermediate Water Formation, and the
729 General Circulation of the Red Sea, Journal of Physical Oceanography, 27, 1233-1257. doi:
730 10.1175/1520-0485(1997)027<1233:CCJCIW>2.0.CO;2, 1997.

731 Eyouni, L., Kokkini, Z., Zarokanellos, N., & Jones, B.. Mechanisms of the Overturning Circulation
732 in the Northern Red Sea [Data set]. Zenodo. https://doi.org/10.5281/zenodo.11046900, 2024.

733 Fairall, C.W., E.F. Bradley, D.P. Rogers, J.B. Edson, G.S. Young: Bulk parameterization of air-sea
734 fluxes for tropical ocean-global atmosphere coupled-ocean atmosphere response experiment, J. Geophys.
735 Res. 101 (C2) 3747–3764 doi: 10.1029/95JC03205, 1996.

736 Falkowski Paul G. et al.,. Biogeochemical Controls and Feedbacks on Ocean Primary
737 Production.Science281,200-206. DOI:10.1126/science.281.5374.200, 1998

738 Garcia H. E., K.W. Weathers, C.R. Paver, I. Smolyar, T.P. Boyer, R.A. Locarnini, M.M. Zweng, A.V.
739 Mishonov, O.K. Baranova, D. Seidov, and J.R. Reagan: World Ocean Atlas 2018, Volume 3: Dissolved
740 Oxygen, Apparent Oxygen Utilization, and Dissolved Oxygen Saturation. A. Mishonov Technical Editor.
741 NOAA Atlas NESDIS 83, 38pp, 2019a.

742 Garcia H.E., K.W. Weathers, C.R. Paver, I. Smolyar, T.P. Boyer, R.A. Locarnini, M.M. Zweng, A.V.
743 Mishonov, O.K. Baranova, D. Seidov, and J.R. Reagan. World Ocean Atlas 2018. Vol. 4: Dissolved
744 Inorganic Nutrients (phosphate, nitrate and nitrate+nitrite, silicate). A. Mishonov Technical Editor,
745 NOAA Atlas NESDIS 84, 35pp, 2019b.

746 GEBCO Bathymetric Compilation Group 2021: The GEBCO_2021 Grid - a continuous terrain model
747 of the global oceans and land. NERC EDS British Oceanographic Data Centre NOC.
748 doi:10.5285/c6612cbe-50b3-0cff-e053-6c86abc09f8f, 2021.

749    Gelaro, R., McCarty, W., Suárez, M. J., Todling, R., Molod, A., Takacs, L., Randles, C. A.,

750    Darmenov, A., Bosilovich, M. G., Reichle, R., Wargan, K., Coy, L., Cullather, R., Draper, C., Akella, S.,

751    Buchard, V., Conaty, A., da Silva, A. M., Gu,

752    W., Kim, G.-K., Koster, R., Lucchesi, R., Merkova, D., Nielsen, J. E., Partyka, G., Pawson, S.,

753    Putman, W., Rienecker, M., Schubert, S. D., Sienkiewicz, M., & Zhao, B.: The Modern-Era Retrospective

754    Analysis for Research and Applications, Version 2 (MERRA-2), *Journal Of Climate*, *30*, 5419-5454,

755    2017.

756    Iselin, C. O. D.: The influence of vertical and lateral turbulence on the characteristics of the waters at

757    mid-depths, Eos, Transactions American Geophysical Union, 20(3). doi 10.1029/TR020i003p00414,

758    1939.

759    Jain, V., Shankar, D., Vinayachandran, P.N. et al.: Evidence for the existence of Persian Gulf Water

760    and Red Sea Water in the Bay of Bengal. Clim Dyn **48,** 3207–3226. doi: 10.1007/s00382-016-3259-4,

761    2017

762    Johnson, K. S., J. N. J. N. Plant, S. C. Riser, and D. Gilbert: Air Oxygen Calibration of Oxygen

763    Optodes on a Profiling Float Array, Journal of Atmospheric and Oceanic Technology, 2160–2172. doi

764    10.1175/JTECH-D-15-0101.1, 2015

765    Karnauskas, K. B., and B. H. Jones: The Interannual Variability of Sea Surface Temperature in the

766    Red Sea From 35 Years of Satellite and In Situ Observations, Journal of Geophysical Research: Oceans,

767    123(8), 5824-5841, doi: 10.1029/2017JC013320, 2018.

768    Kheireddine, M., Dall'Olmo, G., Ouhssain, M., Krokos, G., Claustre, H.,Schmechtig, C., et al.:

769    Organic carbon export and loss rates in the RedSea.Global Biogeochemical Cycles,34,e2020GB006650.

770    doi:10.1029/2020GB006650, 2020

771    Krokos, G., Cerovečki, I., Papadopoulos, V. P., Hendershott, M. C., & Hoteit, I.: Processes governing

772    the seasonal evolution of mixed layers in the Red Sea. Journal of Geophysical Research: Oceans, 127,

773    e2021JC017369. https://doi.org/10.1029/2021JC017369, 2022.

774    Kürten, B., Al-Aidaroos, A. M., Kürten, S., El-Sherbiny, M. M., Devassy, R. P., Struck, U., …

775    Sommer, U. . Carbon and nitrogen stable isotope ratios of pelagic zooplankton elucidate ecohydrographic

features in the oligotrophic Red Sea. *Progress in Oceanography*, 140, 69–90. https://doi.org/10.1016/j.pocean.2015.11.003, 2016.

Kürten, B., Zarokanellos, N. D., Devassy, R. P., El-Sherbiny, M. M., Struck, U., Capone, D. G., et al. Seasonal modulation of mesoscale processes alters nutrient availability and plankton communities in the Red Sea. *Progress in Oceanography*, 173, 238–255. https://doi.org/10.1016/j.pocean.2019.02.007, 2019

Lea, D. J., Mirouze, I., Martin, M. J., King, R. R., Hines, A., Walters, D. and Thurlow, M.: Assessing a new data assimilation system based on the Met Office coupled atmosphere-land-ocean-sea ice model. Monthly Weather Review, 143, 4678-4694,. doi 10.1175/MWR-D-15-0174.1, 2015

Lozier, M. S.: Evidence for large-scale eddy-driven gyres in the North Atlantic, Science, 277(5324), 361– 364, doi: 10.1126/science.277.5324.361, 1997.

Mahadevan A. The Impact of Submesoscale Physics on Primary Productivity of Plankton. Ann Rev Mar Sci. 2016;8:161-84. doi: 10.1146/annurev-marine-010814-015912. 2015

Manasrah, R.. The general circulation and water masses characteristics in the Gulf of Aqaba and northern Red Sea. Ph.D. thesis, Meereswissenschaftliche Berichte Institut für Ostsee Forschung Warnemünde, Universität Rostock, 2002.

Manasrah, Mohammad Badran, Hans Ulrich Lass, and Wolfgang Fennel: Circulation and winter deep-water formation in the northern Red Sea, Oceanoglica, 46(1), 5-23, 2004.

Morcos: Physical and Chemical Oceanography of the Red Sea, Annual Review, 8, 73-202. doi: 10.12691/ajwr-3-3-2

Mohamed B. and Skliris N., Recent sea level changes in the Red Sea: Thermosteric and halosteric contributions, and impacts of natural climate variability. Progress in Oceanography, Vol 231, 103416, https://doi.org/10.1016/j.pocean.2025.103416, 2025.

Morcos, and Soliman (1972), Circulation and deep water formation in the northern Red Sea in winter, *L'Océanographie Physique de la Mer Rouge, UNESCO*, 91–103, 1970

Adele K. Morrison, Darryn W. Waugh, Andrew McC. Hogg, Daniel C. Jones, Ryan P. Abernathey: Ventilation of the Southern Ocean Pycnocline, Annual Review of Marine Science 14:1, 405-430, 2022.

Murray, S. P., and W. Johns: Direct observations of Bab el Mandab Strait, Geophysical Research Letters 24(21), 2557-2560. doi: 10.1029/97GL02741, 1997.

804     OBPG, MODIS Aqua Level 3 SST Thermal IR Daily 4km Daytime v2014.0. Ver. 2014.0.
805     PO.DAAC, CA, USA. Dataset accessed at doi: 10.5067/MODSA-1D4D4, 2015.

806     Papadopoulos, V. P., Y. Abualnaja, S. A. Josey, A. Bower, D. E. Raitsos, H. Kontoyiannis, and I.
807     Hoteit : Atmospheric forcing of the winter air-sea heat fluxes over the northern Red Sea, Journal of
808     Climate, 26, 1685–1701. doi: 10.1175/JCLI-D-12-00267.1, 2013

809     Papadopoulos, V. P., et al.: Factors governing the deep ventilation of the Red Sea, Journal of
810     Geophysical Research: Oceans, 120(11), 7493-7505, doi:10.1002/2015JC010996, 2015.

811     Patzert, W.: Wind-induced reversal in Red Sea circulation, Deep-Sea Research, 21, 109-121.doi:
812     10.1016/0011-7471(74)90068-0, 1974.

813     Price, J., R. Weller, and R. Pinkel: Diurnal Cycling' Observations and Models of the Upper Ocean
814     Response to Diurnal Heating, Cooling, and Wind Mixing Journal of Geophysical Research, 91(C7), 8411-
815     8427. doi: 10.1029/JC091iC07p08411, 1986

816     Quadfasel, D., and H. Baudner: Gyre-scale circulation cells in the Red Sea, Oceanologica Acta, 16(3),
817     221-229, 1993.

818     Raitsos, D. E., Y. Pradhan, R. J. W. Brewin, G. Stenchikov, and H. I.: Remote sensing the
819     phytoplankton   seasonal   succession   of   the   Red   Sea,   PLoS   ONE,   8(6),   e64909.
820     doi:10.1371/journal.pone.0064909, 2013.

821     Rienecker, M. M., et al.: MERRA: NASA's Modern-Era Retrospective Analysis for Research and
822     Applications, journal of Climate, 24(14), 3624-3648, doi:10.1175/JCLI-D-11-00015.1, 2011.

823     Roesler, C., Uitz, J., Claustre, H., Boss, E., Xing, X., Organelli, E., Briggs, N., Bricaud, A.,
824     Schmechtig, C., Poteau, A., D'Ortenzio, F., Ras, J., Drapeau, S., Haëntjens, N., & Barbieux, M:
825     Recommendations for obtaining unbiased chlorophyll estimates from in situ chlorophyll fluorometers: A
826     global analysis of WET Labs ECO sensors, Limnology and Oceanography Methods 15(6), 572-585.doi:
827     10.1002/lom3.10185, .2017.

828     Sanikommu, S., Toye, H., Zhan, P.,Langodan, S., Krokos, G., Knio, O., &Hoteit, I. Impact of
829     atmospheric and model physics perturbations on a high-resolution ensemble data assimilation system of
830     the   Red   Sea.   Journal   of   Geophysical   Research:   Oceans,   125,   e2019JC015611.
831     https://doi.org/10.1029/2019JC015611, 2020.

832 Schott, F. A., and J. P. McCreary: The monsoon circulation of the Indian Ocean, *Progress in*
833 *Oceanography*, *51*(1), 1-123, doi:10.1016/S0079-6611(01)00083-0, 2001.

834 Smeed, D.: Seasonal variation of the flow in the strait of Bab al Mandab, Oceanologica Acta, 20(6),
835 773-781, 1997.

836 Sofianos, S., and W. Johns: An Oceanic General Circulation Model (OGCM) investigation of the Red
837 Sea circulation, 1. Exchange between the Red Sea and the Indian Ocean, Journal of Geophysical Research
838 107(C11), 3196, doi:10.1029/2001JC001184, 2002.

839 Sofianos, S. and W. E. Johns: An Oceanic General Circulation Model (OGCM) investigation of the
840 Red Sea circulation: 2. Three-dimensional circulation in the Red Sea, Journal of Geophysical Research,
841 108(C3), 1-15, doi:10.1029/2001JC001185, 2003.

842 Sofianos, S. and W. E. Johns: Observations of the summer Red Sea circulation, Journal of
843 Geophysical Research, 112(C06025), 1-20, doi:10.1029/2006JC003886, 2007.

844 Sofianos, S. S., W. E. Johns, and S. P. Murray: Heat and freshwater budgets in the Red Sea from
845 direct observations at Bab el Mandeb, Deep-Sea Research Part Ii-Topical Studies in Oceanography, 49(7-
846 8), 1323-1340, doi:10.1016/S0967-0645(01)00164-3, 2002

847 TEOS, SCOR, and IAPSO: The international thermodynamic equation of seawater – 2010:
848 Calculation and use of thermodynamic properties, Intergovernmental Oceanographic Commission,
849 UNESCO, Paris, 196 pp, 2010.

850 Triantafyllou, G., F. Yao, G. Petihakis, K. P. Tsiaras, D. E. Raitsos, and I. Hoteit, Exploring the Red
851 Sea seasonal ecosystem functioning using a three-dimensional biophysical model, Journal of Geophysical
852 Research-Oceans, 119(3), 1791-1811, doi:10.1002/2013jc009641, 2014.

853 Werdell, P. J., et al.: Generalized Ocean color inversion model for retrieving marine inherent optical
854 properties, Appl Optics, 52(10), 2019-2037, doi:10.1364/Ao.52.002019, 2013.

855 Williams R.G., Meijers A.: Ocean subduction, Cochran J.K., Bokuniewicz H.J., Yager P.L. (Eds.),
856 Encyclopedia of Ocean Sciences (3rd ed.), Academic Press, Cambridge, Massachusetts, United States,
857 pp. 141-157, 10.1016/B978-0-12-409548-9.11297-7, 2019

858 Woelk, S., and D. Quadfasel: Renewal of deep water in the Red Sea during 1982-1987, Journal of
859 Geophysical Research-Oceans, 101(C8), 18155-18165, doi:10.1029/96jc01148, 1996.

Yao, F., and I. Hoteit (2018), Rapid Red Sea Deep Water renewals caused by volcanic eruptions and the North Atlantic Oscillation, *Science Advances 4*(6), doi:10.1126/sciadv.aar5637.

Yao, F., I. Hoteit, L. J. Pratt, A. S. Bower, P. Zhai, A. Köhl, G. Gopalakrishnan: Seasonal overturning circulation in the Red Sea: 1. Model validation and summer circulation, J. Geophys. Res. Oceans,119, doi:10.1002/2013JC009004, 2014a.

Yao, F., I. Hoteit, L. J. Pratt, A. S. Bower,A. Köhl, G. Gopalakrishnan, and D.Rivas : Seasonal overturning circulation in the Red Sea: 2. Winter circulation,J. Geophys. Res. Oceans,119, 2263–2289, doi:10.1002/2013JC009331, 2014b.

Zarokanellos, N. D., B. Kürten, J. H. Churchill, C. Roder, C. R. Voolstra, Y. Abualnaja, and B. H. Jones: Physical Mechanisms Routing Nutrients in the Central Red Sea, Journal of Geophysical Research: Oceans, 122, doi:10.1002/2017JC013017, 2017a.

Zarokanellos, N. D., V. P. Papadopoulos, S. S. Sofianos, and B. H. Jones: Physical and biological characteristics of the winter-summer transition in the Central Red Sea, Journal of Geophysical Research-Oceans, 122(8), 6355-6370,doi:10.1002/2017jc012882, 2017b.

Zarokanellos, N., and B. H. Jones: Winter mixing, mesoscale eddies and eastern boundary current: Engines for biogeochemical variability of the central Red Sea during winter/early spring period., Journal of Geophysical Research-Oceans, accepted, doi:10.1029/2020JC016714, 2021.

Zarokanellos, N. D., Rudnick, D. L., Garcia-Jove, M., Mourre, B., Ruiz, S., Pascual, A., & Tintoré, J.. Frontal dynamics in the Alboran Sea: 1. Coherent 3D pathways at the Almeria-Oran front using underwater glider observations. Journal of Geophysical Research: Oceans, 127, e2021JC017405. https://doi. org/10.1029/2021JC017405, 2022.

Zhai, P., A. S. Bower, W. M. S. Jr., and L. J. Pratt: Formation and spreading of Red Sea Outflow Water in the Red Sea, Journal of Geophysical Research, 120(9), 6542-6563, doi:10.1002/2015JC010751, 2015.

Zhan, P., G. Gopalakrishnan, A. C. Subramanian, D. Guo, and I. Hoteit: Sensitivity Studies of the Red Sea Eddies Using Adjoint Method, Journal of Geophysical Research: Oceans, 123, doi:10.1029/2018JC014531, 2018.

Zhan, P., G. Krokos, D. Q. Guo, and B. Hoteit: Three-Dimensional Signature of the Red Sea Eddies

888 and Eddy-Induced Transport, Geophysical Research Letters, 46(4), 2167-2177,
889 doi:10.1029/2018gl081387, 2019.

890 Zhan, P., A. C. Subramanian, F. Yao, and I. Hoteit: Eddies in the Red Sea: A statistical and dynamical
891 study, Journal of Geophysical Research: Oceans, 119(6), 3909-3925, doi:10.1002/2013JC009563, 2014.

892 Zhan, P., A. C. Subramanian, F. Yao, A. R. Kartadikaria, D. Guo, and I. Hoteit: The eddy kinetic
893 energy budget in the Red Sea, Journal of Geophysical Research, 121(7), 4732-4747, doi:
894 10.1002/2015JC011589, 2016.

895 Zhang, Z., and J. C. Moore: *Mathematical and Physical Fundamentals of Climate Change*, Elsevier,
896 doi: 10.1016/B978-0-12-800066-3.00006-1, 2015.